


Genetic architecture of bone marrow fat fraction implies its involvement in osteoporosis risk

Received: 9 November 2024

Accepted: 1 August 2025

Published online: 12 August 2025

 Check for updates

Zuyou Wu^{1,6}, Yang Yang^{2,6}, Caibo Ning^{1,6}, Jiali Li^{2,6}, Yimin Cai³, Yanmin Li³, Zilong Cao³, Shuangshuang Tian³, Jingyi Peng³, Qianying Ma³, Chunyi He³, Shuting Xia³, Jun Chen⁴, Xiaoping Miao¹, Zhen Li²✉, Ying Zhu¹✉, Qian Chu⁵✉ & Jianbo Tian¹✉

Bone marrow adipose tissue, as a distinct adipose subtype, has been implicated in the pathophysiology of skeletal, metabolic, and hematopoietic disorders. To identify its underlying genetic factors, we utilized a deep learning algorithm capable of quantifying bone marrow fat fraction (BMFF) in the vertebrae and proximal femur using magnetic resonance imaging data of over 38,000 UK Biobank participants. Genome-wide association analyses uncovered 373 significant BMFF-associated variants (P -value $< 5 \times 10^{-9}$), with enrichment in bone remodeling, metabolism, and hematopoiesis pathway. Furthermore, genetic correlation highlighted a significant association between BMFF and skeletal disease. In about 300,000 individuals, polygenic risk scores derived from three proximal femur BMFF were significantly associated with increased osteoporosis risk. Notably, Mendelian randomization analyses revealed a causal link between proximal femur BMFF and osteoporosis. Here, we show critical insights into the genetic determinants of BMFF and offer perspectives on the biological mechanisms driving osteoporosis development.

Bone marrow adipose tissue (BMAT) derives from mesenchymal lineage cells within the bone marrow¹ and may play an active role in regulating skeletal remodeling². Specifically, BMAT can influence osteoblast differentiation through a competitive differentiation pathway³, potentially leading to osteoporosis. Additionally, recent studies suggest that BMAT, as a complex and dynamic fat depot, may contribute to the development of common diseases such as diabetes^{4,5}, obesity⁶, and anorexia nervosa⁷. Moreover, BMAT are also involved in hematopoietic regulation and can promote the survival and regeneration of hematopoietic stem cells by secreting stem cell

factors^{8,9}. Therefore, BMAT emerges as a potential endophenotype in multisystem diseases, and the exploration of its genetic architecture may offer a fresh perspective on the mechanisms underlying the occurrence of these diseases.

Magnetic resonance imaging (MRI) is one of the most widely used medical imaging modalities for quantifying BMAT phenotypes due to its noninvasive and versatile nature¹⁰. Specifically, chemical shift-encoding-based water-fat separation methods are employed to calculate the bone marrow fat fraction (BMFF)¹¹. However, the process of manually delineating bone marrow regions is prone to significant

¹Department of Epidemiology and Biostatistics, School of Public Health, State Key Laboratory of Metabolism and Regulation in Complex Organisms, TaiKang Center for Life and Medical Sciences, Wuhan University, Wuhan, China. ²Department of Radiology, Tongji Hospital, Tongji Medical College, Huazhong University of Science and Technology, Wuhan, China. ³Department of Epidemiology and Biostatistics, School of Public Health, Wuhan University, Wuhan, China. ⁴Bayer Healthcare, Wuhan, China. ⁵Department of Oncology, Tongji Hospital, Tongji Medical College, Huazhong University of Science and Technology, Wuhan, China. ⁶These authors contributed equally: Zuyou Wu, Yang Yang, Caibo Ning, Jiali Li. ✉e-mail: zhenli@hust.edu.cn; zhuying@whu.edu.cn; qianchu@tjh.tjmu.edu.cn; tianjb@whu.edu.cn

errors, poor reproducibility, and is highly time-consuming, especially when quantifying large sample sizes. These challenges have posed significant obstacles to the accurate estimation of BMFF in large-scale studies. To enable large-scale genome-wide association study (GWAS) of BMFF imaging phenotypes and explore the relationship between BMAT and diseases through multiple strategies, we utilized a deep learning algorithm, the integrated bone marrow automatic segmentation and fat fraction calculation strategy (IBAS-FFCS), to accurately estimate BMFF. We quantified the BMFF of a large cohort population from the UK Biobank (UKB), which provides both high-quality standardized MRI data and genotype information, offering a unique opportunity to explore the genetic determinants of BMFF traits.

In this work, we aimed to investigate the genetic architecture of 15 BMFF traits, including the BMFFs of the thoracic vertebrae (Th8–Th12), lumbar vertebrae (L1–L5), and the left and right proximal femur (LPF and RPF) and the average BMFFs of these three anatomical sites expressed as Th, L, and PF, respectively (Fig. 1a). Using the deep learning-based method mentioned above, we first performed GWAS on these 15 BMFF traits in more than 38,000 UKB participants. We then conducted variants-to-genes analyses to explore the biological significance of the GWAS findings, with a focus on the genomic distribution of identified loci and the genes that significantly influence multiple BMFF traits. Following this, we assessed the genetic associations between the 15 BMFF traits and a range of skeletal, metabolic and hematopoietic diseases through genetic correlation analyses. We

further developed polygenic risk scores (PRS) based on BMFF traits and validated their predictive ability for these diseases in approximately 300,000 individuals. Finally, we further leveraged Mendelian randomization (MR) to evaluate causal connections between BMFF and osteoporosis.

Results

Integrated bone marrow automatic segmentation and fat fraction calculation strategy

Utilizing the available whole-body MRI available in the UKB, our IBAS-FFCS procedure enables precise calculation of BMFF, with its basic process illustrated in Fig. 1b. To achieve state-of-the-art performance in segmentation tasks, a random sample of 406 subjects for the vertebra and 257 subjects for the proximal femur were extracted from the UKB database and annotated by three experienced radiologists. These datasets were then randomly divided into training, validation, and testing sets using a 7:3:3 ratio.

In the testing dataset, the dice coefficients of IBAS-FFCS were greater than 0.863, and the intraclass correlation coefficients (ICCs) between manual segmentation and IBAS-FFCS were greater than 0.970 (Supplementary Data 1). In addition, Dixon whole-body images of 180 external subjects collected from our own research institution (Supplementary Methods and Supplementary Data 2) were used to independently evaluate the performance of IBAS-FFCS, resulting in ICCs consistently exceeding 0.9. Altogether, these results confirmed that

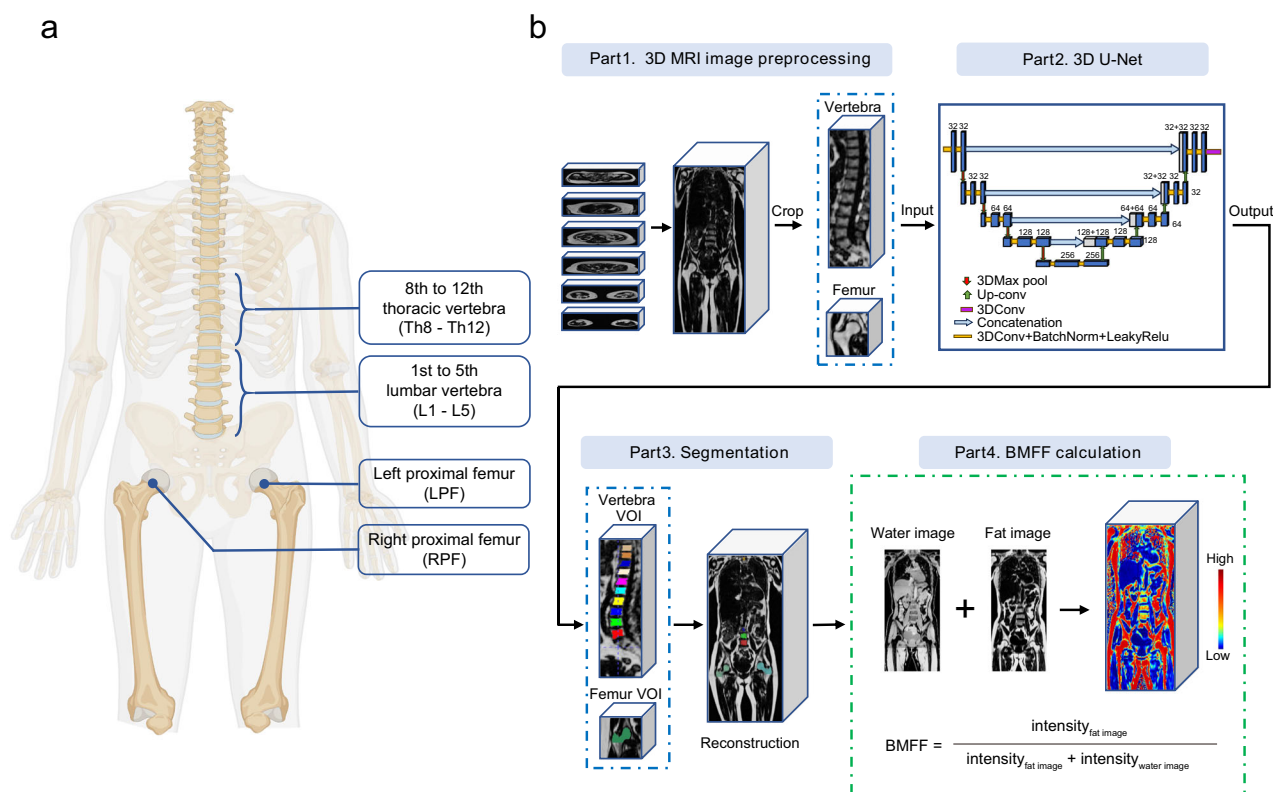


Fig. 1 | Integrated bone marrow automatic segmentation and fat fraction calculation strategy (IBAS-FFCS). **a** IBAS-FFCS can calculate the fat fraction of the 8th to 12th thoracic vertebra, the 1st to 5th lumbar vertebra, and the proximal femur on both sides. **b** Part1. This study aligned and concatenated the six 3D 2-point Dixon MRI images and applied image enhancement strategies such as scaling intensity and random flipping to the images. All data were cropped according to the bounding box of the spine and femur, and then fed into the 3D-Unet model. Part2. The preprocessed images were fed into a deep learning 3D-Unet model for training, leveraging a GPU server equipped with an NVIDIA RTX 4090D GPU. The U-Net segmentation algorithm was continuously optimized based on the Dice loss

function and the Adam algorithm. The topology of the whole network consists of the encoding and decoding subnetworks. Four stages in encoding and decoding counterparts indicate that four-level scales of feature maps were formulated for automatic feature extraction. Part3. The 3D-Unet outputted visual masks of the femur and spine, with different colors representing the left and right femurs, as well as the spine from L1 to Th8. Part4. The volume of interest (VOI) for the spine and femurs was extracted and transferred to the fat and water images of the two-point Dixon sequence, where the bone marrow fat fraction is calculated based on a computational formula. Panel a was created in BioRender. Wu, Z. (2025) <https://BioRender.com/qdjy0e>.

the performance of IBAS-FFCS is comparable to that of radiologists. The detailed results of each dataset are presented in Supplementary Data 1. In addition, we performed inter-reader and model-reader variability analyses in 30 UKB subjects and observed a high consistency (Supplementary Data 3, 4).

The completed model was applied to 51,487 participants within UKB for whom MRI data were available, resulting in 15 BMFFs for each participant. It must be noted that during application, the model yielded an average of 196 zero or missing vertebral BMFF data and an average of 62 zero or missing femoral BMFF (Supplementary Data 5). We randomly selected 200 cases with zero or missing data for manual inspection. Based on this assessment, we summarized the segmentation error into four primary categories: (1) imaging artifacts; (2) fusion image errors; (3) individual differences such as bone-related diseases or skeletal developmental abnormalities; and (4) image inversion (Supplementary Fig. 1).

The original 51,487 samples were screened, yielding participants ranging from 38,522 to 39,178 as study subjects (Method, Supplementary Fig. 2), whose characteristics are recorded in Supplementary Data 6. To ensure the normality of the data, we performed the rank-based inverse normal transformation of the residuals of BMFFs (Supplementary Fig. 3). Further, we performed a principal component analysis (PCA) and found that the first three principal components (PC) could collectively explain 90.4% of the total variance (Supplementary Fig. 4), and we therefore applied Bonferroni corrections on downstream analyses based on these three components to prevent overly conservative correction.

To validate the reliability of BMFF measurements, we examined the associations between BMFF and sex, age, ethnicity, body mass index (BMI), bone mineral density (BMD), and total body fat mass. The result revealed that vertebral BMFF was lower in males compared to females, while femoral BMFF was higher in males (Supplementary Fig. 5). Both vertebral and femoral BMFF increased with age (Supplementary Fig. 6). In addition, ethnic differences were observed, with individuals of White ethnicity exhibiting higher BMFF compared to other ethnic groups (Supplementary Fig. 7). As expected, both vertebral and femoral BMFF were negatively associated with BMD (Supplementary Fig. 8). Femoral BMFF showed a negative correlation with BMI, whereas vertebral BMFF was positively correlated with BMI (Supplementary Data 7). Total body fat mass was positively correlated with BMFF at all sites, with a stronger association observed for vertebral BMFF compared to femoral BMFF (Supplementary Data 7). These findings are consistent with previously published studies^{12–14}, supporting the reliability of our BMFF measurements.

Genome-wide association studies of bone marrow fat fraction

To understand the common genetic basis for variation in BMFF, we performed a series of GWAS on 15 BMFF with a maximum sample size of 39,178 individuals. In total, we identified 405 independent significant variants ($r^2 < 0.1$) (Supplementary Data 8) and 373 lead variant ($r^2 < 0.05$) (Supplementary Data 9) associated with 15 BMFFs (P value $< 5 \times 10^{-9}$), including 35 for Th, 30 for L, and 26 for PF, among others, involving 133 unique lead variants (Fig. 2 and Supplementary Figs. 9, 10). Notably, 78 of the lead variants was shared across at least two BMFF traits, highlighting a degree of overlap in the genetic architecture of BMFF. For example, rs55953331 in the *LEPR* gene reaches genome-wide significance in BMFF of Th8, Th9, Th10, and Th.

We conducted three sensitivity analyses (Methods) to assess the robustness of the primary 15 GWASs. Firstly, we performed sex-stratified GWASs and found that the Manhattan plots for most of the 15 traits were very similar (Supplementary Fig. 11), and the number of lead variants was comparable across the traits (Supplementary Fig. 12 and Supplementary Data 10). Additionally, we performed a correlation analysis between the beta coefficients of the lead variants for each trait in both sexes, which showed significant correlation (0.87–0.98). We

also performed Sex×Genotype interaction analysis, which did not find P-sex genome-wide significant for any of the lead variants in 15 BMFFs (Supplementary Data 11). Furthermore, we randomly divided the entire population into two subsets at a 7:3 ratio (sex and age matched) and performed GWASs separately in each subset. The results demonstrated strong robustness, with highly correlated effect sizes between the two subsets ($0.88 < r < 0.98$ for Pearson's r) and no significant differences ($P > 0.98$ for two-sample t -test) (Supplementary Fig. 13 and Supplementary Data 12), further supporting the absence of cryptic population stratification in our primary GWASs. Additionally, to evaluate the influence of BMI adjustment on the BMFF GWAS, we compared the results with and without BMI adjustment and observed no substantial differences in the genetic associations ($r > 0.99$ for Pearson's r ; $P > 0.99$ for two-sample t -test) (Supplementary Fig. 14 and Supplementary Data 13), indicating that BMI adjustment did not significantly alter the findings.

Functional characterization of risk variants

We defined variants that were in linkage disequilibrium ($r^2 \geq 0.1$) with any independent significant variant as candidate variants and further functionally annotated these variants using functional mapping and annotation of the GWAS (FUMA) online platform¹⁵. The number of candidate variants ranged from 5116 in L1 to 7838 in Th, most of which were located in intronic and intergenic regions (Fig. 3a). Subsequently, we investigated whether these candidate variants were enriched among genetic regulatory elements. For a majority of BMFFs, the enrichment analysis revealed the remarkable enrichment of candidate variants in histone markers of enhancers (H3K4me1 and H3K27ac), promoters (H3K4me3) and active transcription (H3K36me3 and H3K9ac), but significant depletion in repressive transcription (H3K27me3 and H3K9me3) (Fig. 3b). In addition, based on the current knowledge, we assumed that BMFF and possibly related diseases (such as osteoporosis, diabetes, etc.) have a common genetic structure, so we analyzed the enrichment of candidate variants in disease risk loci. Results showed that candidate variants were significantly enriched in GWAS significant loci of osteoporosis, fracture, anorexia nervosa, type 2 diabetes, nonalcoholic fatty liver disease, and multiple myeloma (Fig. 3c and Supplementary Data 14). Also, significant enrichment of candidate variants was observed in risk loci associated with BMFF-related traits, such as BMD and waist-hip ratio (WHR) (Supplementary Fig. 15 and Supplementary Data 15). Notably, this enrichment reflects shared genetic architecture at the locus level but does not imply concordance in effect directions.

Gene mapping and functional enrichment

We further sought to identify candidate genes influencing BMFF variation by combining evidence from four strategies: physical positional, expression quantitative trait locus (eQTL) association, multi-marker analysis of genomic annotation (MAGMA), and transcriptome-wide association study (TWAS). A total of 409 mapped genes associated with the 15 BMFF were identified, of which 82 genes were found by positional mapping (Supplementary Data 9), 178 genes by eQTL mapping (Supplementary Data 16), 186 genes by MAGMA mapping (Supplementary Data 17), and 110 genes by TWAS mapping (Supplementary Data 18 and Supplementary Fig. 16). When the susceptibility genes of each BMFF were combined, there were 12 genes mutually implicated by all four methods (Supplementary Fig. 17a). When the genes identified by the four methods were combined, five unique genes were found to be shared among 15 BMFFs (Supplementary Fig. 17b). Among these genes, *GSDMA* was labeled by at least three methods in 15 BMFFs, and the gene encodes a protein that is a family of pore-forming proteins that cause pyroptosis, which is associated with increased osteoclasts, increased bone resorption, and reduced bone mineralization. In addition, other noteworthy genes identified through multiple methods include a BMD-related gene *CCDC170*, *PPAR γ*

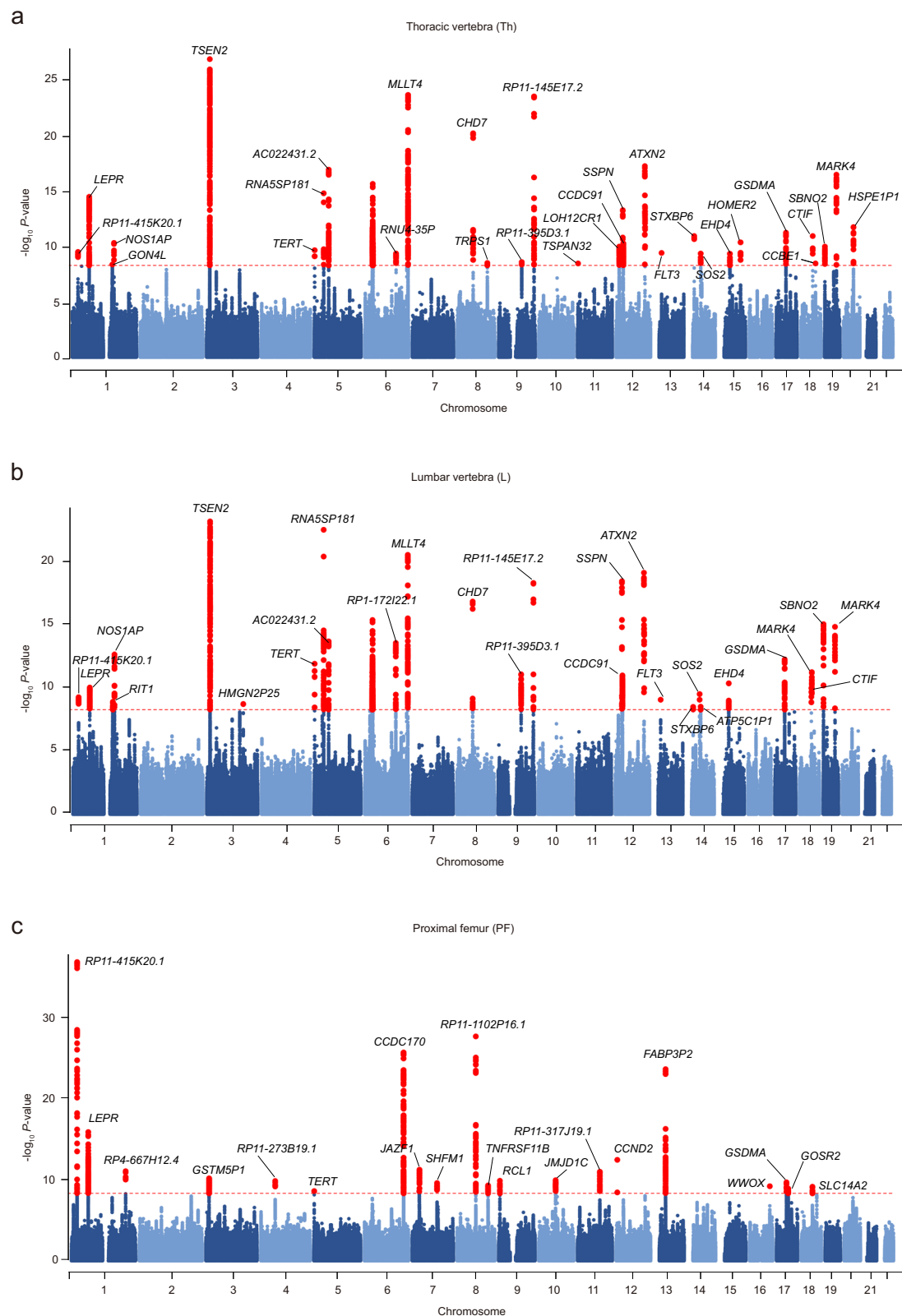
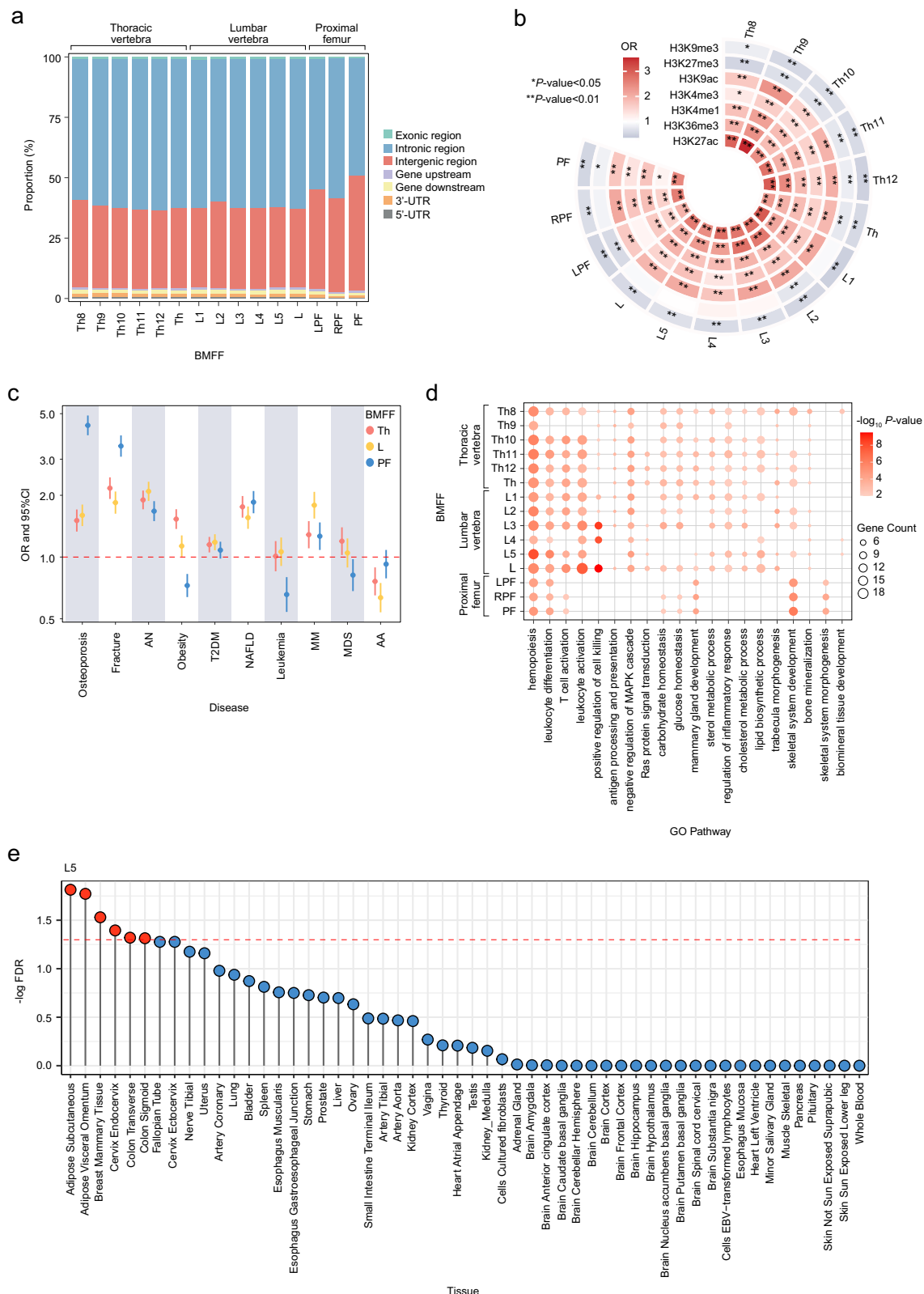


Fig. 2 | Genome-wide association studies results for three representative BMFFs. Manhattan plots show the chromosomal position on the x-axis and the $-\log_{10} P$ value on the y-axis for the GWAS result of BMFF of Th (a), L (b), and PF (c). The red solid line indicates the genome-wide significance threshold at $P < 5 \times 10^{-9}$. Loci that contain significant variants were labeled with the name of the nearest gene. P value are two-sided based on the chi-squared test statistics in

the BOLT-LMM software. The genome-wide significance threshold at $P < 5 \times 10^{-9}$ was determined using a conservative Bonferroni correction, in which 0.05 was divided by the total number of SNPs analyzed in our GWAS (8,412,349), yielding approximately 5×10^{-9} . BMFF bone marrow fat fraction, Th thoracic vertebra, L lumbar vertebra, PF proximal femur.



involved in the differentiation of bone marrow mesenchymal stem cells and *LEPR* encoding leptin receptor. Other susceptibility genes are summarized in Supplementary Fig. 18 and Supplementary Data 19.

Subsequently, we conducted gene ontology (GO) enrichment analyses to gain a comprehensive understanding of the functions of these susceptible genes. As expected, these genes showed significant enrichment in several functional categories, including skeletal system

development, trabecula morphogenesis, glucose homeostasis, lipid biosynthetic process, and hematopoiesis (Fig. 3d and Supplementary Data 20). These findings suggest a close functional link between bone marrow adipose tissue and skeletal, metabolic, and hematopoietic systems, while the causal relationships remain to be elucidated. Furthermore, the tissue-specific gene expression analysis revealed that. Across 54 human organ tissues, most genes were overexpressed in

Fig. 3 | Functional characterization for risk variants of 15 BMFFs and pathway enrichment and tissue enrichment for susceptible genes of 15 BMFFs. **a** Bar chart represents the proportions for risk variants of 15 BMFFs annotated with each functional category (intron region, gene upstream, and downstream regions, intergenic region, 3'-UTR, 5'-UTR and exon region). **b** Enrichment analyses for risk variants of 15 BMFFs among regions of histone modification, such as H3K4 monomethylation marks (H3K4me1), H3K4 trimethylation marks (H3K4me3), H3K27 acetylation marks (H3K27ac), H3K36 trimethylation marks (H3K36me3), and H3K9 trimethylation marks (H3K9me3). *P* value was calculated by two-tailed Fisher's exact test. **c** Enrichment analyses for risk variants of thoracic vertebra, lumbar vertebra and proximal femur mean BMFF, respectively, among ten related disease risk loci. The number of candidate variants used was 7838 for Th, 7621 for L, and 7149 for PF. The number of control variants used was 7258 for Th, 7056 for L, and 6.646 for PF. *P* value was calculated by two-tailed Fisher's exact test. The error bars

represent the 95% confidence interval. **d** Pathway enrichment analyses of Gene Ontology terms were performed at <http://kobas.cbi.pku.edu.cn>. Significantly enriched GO terms (unadjusted *P* < 0.05, two-sided) were identified from the analyses of significant genes for BMFF. Unadjusted *P* values were calculated by two-tailed Fisher's exact test. **e** Tissue expression result for 54 specific tissue types was obtained from GTEx v8 using FUMA. FDR < 0.05 was considered statistically significant. Only the result for L5 is shown here. BMFF bone marrow fat fraction, Th thoracic vertebra, L lumbar vertebra, PF proximal femur, LPF left proximal femur, RPF right proximal femur, 3'-UTR 3'-untranslated region, 5'-UTR 5'-untranslated region, H3K4me1 H3K4 monomethylation marks, H3K4me3 H3K4 trimethylation marks, H3K27ac H3K27 acetylation marks, H3K36me3 H3K36 trimethylation marks, H3K9me3 H3K9 trimethylation markers, OR odds ratio, CIs confidence intervals, AN anorexia nervosa, T2DM type 2 diabetes, MM multiple myeloma, MDS myelodysplastic syndrome, AA aplastic anemia.

adipose subcutaneous and adipose visceral omentum, with secondary expression hotspots detected in breast mammary tissue, cervix endocervix, and colon transverse. (Fig. 3e and Supplementary Data 21).

In addition, based on sex-stratified GWAS, sex-specific genes associated with Th, L and PF were identified using four strategies (physical positional, eQTL, MAGMA and TWAS) (Supplementary Data 22). In males, 33 male-specific genes were detected, including *SBNO2*, *HK1*, *CCND2*, *TERT*, *CCDC91*, and *CTSB*, which were consistently identified by at least two methods, with *TERT*, *ATXN2*, *NTN1*, *CTSB*, and *EHD4* showing associations with at least two BMFF sites. Among females, 42 female-specific genes were identified, of which *VMPI*, *MED24*, *SSPN*, and *JAZF1* were replicated by at least two methods, while *VMPI*, *LEPROT*, *HLA-C*, *SLC44A4*, and *EHMT2* demonstrated associations with at least two BMFF sites.

Colocalization

We conducted colocalization analyses to assess whether genetic variants associated with BMFF influence gene expression in mesodermal tissues (subcutaneous and visceral adipose tissue, skeletal muscle) and lymphoid tissues (spleen and lymphocytes). As shown in Supplementary Data 23, strong evidence of colocalization (PPH4 > 0.98) was observed for *GSDMA* in subcutaneous adipose tissue, visceral omentum adipose tissue, skeletal muscle tissue, and spleen tissue across most vertebral and femoral BMFF GWAS. Notably, *GSDMA* was also identified through at least three independent approaches in previous analyses. In femoral BMFF GWAS, we detected colocalization signals (PPH4 > 0.80) for *CCDC170*, *REER*, *ME3*, *PSMD3*, *JAZF1*, and *PPARG*. Similarly, in vertebral BMFF GWAS, significant colocalizations (PPH4 > 0.80) were identified for *EHD4*, *PSMD3*, *THA1P*, *MAPK4*, *MKRN2*, *MLLT4*, *MSTO2P*, *DAP3*, *RAFI*, *NCAPD3*, *CYP19A1*, *RITI*, and *CCBE1*. Most of these genes were supported by at least two independent gene mapping strategies in prior analyses, reinforcing their potential functional relevance. Strikingly, two genes (*RAFI* and *CYP19A1*) were also implicated in BMFF regulation by a previous study, further validating our findings¹⁴.

Heritability and genetic correlation of bone marrow fat fraction

Using summary statistics, we applied linkage disequilibrium score regression (LDSC)³⁶ to estimate the heritability of 15 BMFFs and genetic correlation among these BMFF. The mean heritability (h^2) was 0.20 for the 15 traits (ranging from $h^2 = 0.16$ for L5 to $h^2 = 0.23$ for Th; Fig. 4a). Of significant note were the robust genetic correlations observed within the same type of BMFFs, such as between vertebral BMFFs, the genetic correlation coefficient (r_g) ranged from 0.88 to nearly 1.00 (Fig. 4b bottom triangle). However, there was relatively low genetic correlation between vertebral and femoral BMFFs, ranging from 0.28 to 0.41 (Fig. 4b bottom triangle). In addition, the phenotypic correlation coefficient (r_p) among the 15 BMFFs were calculated. We observed a high degree of agreement between genetic and phenotypic correlations, also as shown by strong correlations between the same types of

BMFFs (r_p range: 0.68–0.96) and relatively low correlations between vertebral and femoral BMFF (r_p range: 0.29–0.39) (Fig. 4b top triangle). These intriguing observations may reflect genetic effects discriminately acting on the BMFFs of different sites, which further manifests at the phenotypic level.

Building on this groundwork, we extended our inquiry to explore the genetic connections between the BMFF and 13 skeletal, metabolic and hematopoietic clinical measures (Supplementary Data 24). Noteworthy negative associations between 15 BMFFs and BMD (r_g range: -0.20 to -0.30) were unearthed (Fig. 4c and Supplementary Data 25). This reinforces the functional interplay between the BMFF and the bone homeostasis, implying a relationship between BMFF and osteoporosis. Further, we observed that multiple BMFFs exhibited negative genetic correlations with hemoglobin (r_g range: -0.12 to -0.16), in contrast to the positive genetic correlations observed between vertebra and triglycerides (r_g range: 0.18–0.24). Collectively, these findings support the justification for investigating the genetics of BMFF as a complementary gateway to understanding the skeletal development, metabolic and hematopoietic processes.

To examine shared genetic effects between BMFF traits and skeletal, metabolic and hematopoietic diseases. We further performed genetic correlation analyses with GWAS summary statistics from 10 related diseases (Supplementary Data 24). As expected, we observed statistically positive genetic correlations of 15 BMFFs with osteoporosis (r_g range: 0.23–0.33; Fig. 4c and Supplementary Data 26). Similarly, r_g for fracture ranged from 0.18 to 0.26, which is consistent with the results for osteoporosis. These findings provide genetic evidence supporting the probable involvement of BMFF in skeletal disease pathophysiology, suggesting that alterations of BMFF may contribute to both osteoporosis and fracture risk.

Polygenetic risk scores for osteoporosis risk stratification

To further explore the relationship between BMFF and diseases, we formulated a PRS of BMFF by incorporating genetic dosage weights based on the effect sizes of independent genetic variants (*P* value < 1×10^{-5} , $r^2 < 0.1$, kb = 250) derived from the corresponding BMFF GWAS results (Supplementary Data 27). Then, we evaluated the ability of PRSs to discriminate corresponding BMFFs. As shown in Fig. 5a–c and Supplementary Fig. 19, higher PRSs tend to higher BMFFs. In addition, multiple linear regression adjusted for age, sex, BMI, and BMD also showed a positive correlation between PRS and BMFF with a beta range from 0.20 to 0.24 (Supplementary Data 28), which proved the validity of our formulated PRS.

Subsequently, we explored whether these PRS of BMFF are able to affect ten diseases incidences. We calculated hazard ratio (HR) and 95% CI using Cox proportional-hazards regression models in a cohort of the remaining about 300,000 UKB white participants that were not included in the former GWASs. As shown in Fig. 5d–f, compared to the other individuals, individuals with the high PRS derived from LPF, RPF and PF BMFF had an increased risk of osteoporosis ($HR_{LPF} = 1.12$, 95%CI_{LPF}:

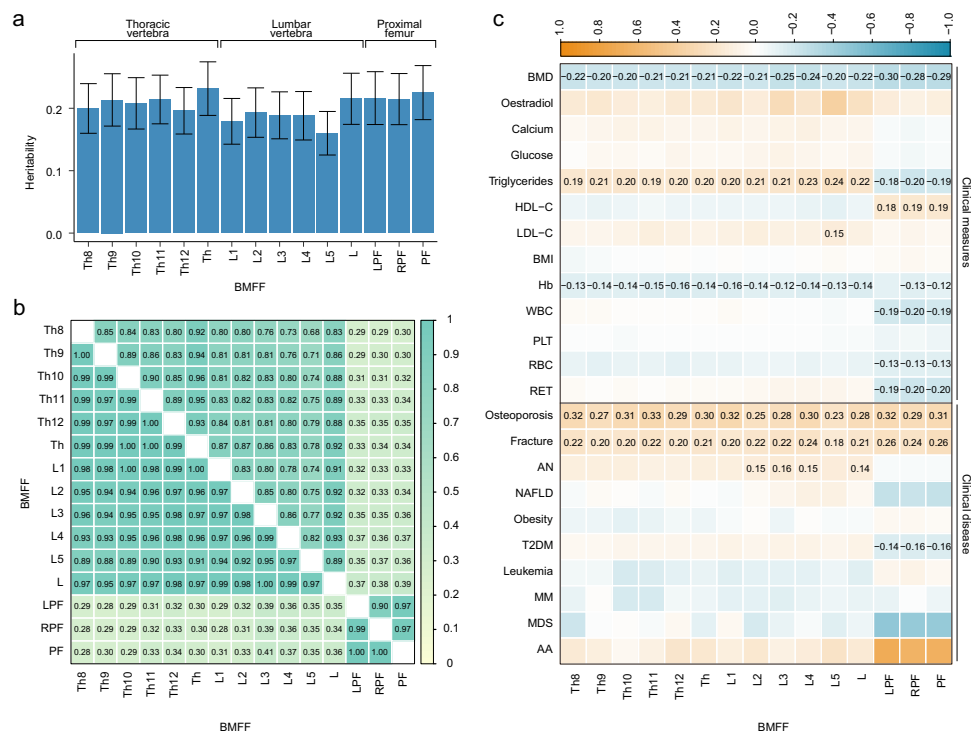


Fig. 4 | SNP heritability and genetic correlations. a Bar chart represents the SNP heritability of 15 BMFFs. The error bars represent the 95% confidence interval. The heritability was calculated using LDSC based on 1,097,459 independent SNPs from GWAS summary statistics, of the following sample sizes: Th8 ($N = 39,007$), Th9 ($N = 38,937$), Th10 ($N = 39,144$), Th11 ($N = 39,178$), Th12 ($N = 39,172$), Th ($N = 38,715$), L1 ($N = 39,030$), L2 ($N = 39,151$), L3 ($N = 39,162$), L4 ($N = 39,121$), L5 ($N = 39,134$), L ($N = 38,897$), LPF ($N = 38,559$), RPF ($N = 38,560$), and PF ($N = 38,522$). **b** The heatmap shows genetic correlations (bottom triangle) and phenotypic correlations (top triangle) between 15 BMFFs. Degree of correlation is indicated by the color legend, ranging from -1 to $+1$. Two-sided P values shown unadjusted are estimated using LDSC for genetic correlation. **c** Genetic correlations between 15 BMFFs and 13 clinical measures and ten clinical diseases. Degree of correlation is indicated by the color legend, ranging from -1 to $+1$. Two-sided P values shown are estimated using

LDSC for genetic correlation. Only the correlation coefficient that survived Bonferroni correction is shown. P value $< 1.28 \times 10^{-3}$ (0.05 divided by 13 clinical measures and three principal components) was considered statistically significant for analysis between BMFFs and measures. P value $< 1.67 \times 10^{-3}$ (0.05 divided by ten clinical diseases and three principal components) was considered statistically significant for analysis between BMFFs and diseases. The exact P values were provided in Supplementary Data 25, 26. BMFF bone marrow fat fraction, Th thoracic vertebra, L lumbar vertebra, PF proximal femur, LPF left proximal femur, RPF right proximal femur, BMD bone mineral density, HDL-C high density lipoprotein cholesterol, LDL-C low density lipoprotein cholesterol, BMI body mass index, Hb hemoglobin concentration, WBC white blood cell count, PLT platelet count, RBC red blood cell count, RET reticulocyte count, AN anorexia nervosa, T2DM type 2 diabetes, MM multiple myeloma, MDS myelodysplastic syndrome, AA aplastic anemia.

1.07–1.18, P value $= 1.06 \times 10^{-6}$, $P_{\text{Log-rank}} = 3.38 \times 10^{-5}$; $\text{HR}_{\text{RPF}} = 1.13$, 95% CI_{RPF} : 1.08–1.18, P value $= 5.01 \times 10^{-7}$, $P_{\text{Log-rank}} = 1.14 \times 10^{-5}$; $\text{HR}_{\text{PF}} = 1.13$, 95% CI_{PF} : 1.08–1.19, P value $= 1.71 \times 10^{-7}$, $P_{\text{Log-rank}} = 7.54 \times 10^{-6}$. This demonstrates that PRS derived from proximal femur BMFF indeed owns significant association with osteoporosis incidence. However, no relationship was observed between PRS derived from vertebral BMFF and the incidence of osteoporosis. Characteristics of the osteoporosis cohort population are recorded in Supplementary Data 6. Detailed results of the Cox regression analysis are provided in Supplementary Data 29. To evaluate the predictive ability of PRS for the onset of osteoporosis, the receiver operating characteristic (ROC) curve and calibration plot were drawn, and a series of indicators including area under the curve (AUC), C-statistic, akaike information criterion (AIC), bayesian information criterion (BIC), R^2 , net reclassification improvement (NRI) and integrated discrimination improvement (IDI) were calculated. As depicted in Supplementary Fig. 20, the results showed that BMFF PRS had limited predictive power for osteoporosis (AUC = 0.532–0.533, C = 0.528–0.530, R^2 = 0.011–0.016). Interestingly, an improvement is noted after further integrating the relevant PRS with other clinical risk factors (AUC = 0.783–0.785, NRI = 0.424, IDI = 0.007). In summary, elevated BMFF demonstrates a significant association with increased osteoporosis risk. However, the predictive utility of BMFF PRS for osteoporosis risk assessment requires further refinement and validation.

Mendelian randomization for the causal relationship between BMFFs and osteoporosis

To verify the potential causation between BMFF and osteoporosis, a two-sample Mendelian randomization analysis was performed. As shown in Fig. 6 and Supplementary Data 30, we observed that several BMFFs were causally associated with osteoporosis, among which proximal femur BMFF show positive causally association ($\text{OR}_{\text{LPF}} = 1.45$, 95% CI_{LPF} : 1.11–1.88, P value $= 5.62 \times 10^{-4}$; $\text{OR}_{\text{RPF}} = 1.47$, 95% CI_{RPF} : 1.12–1.94, P value $= 6.26 \times 10^{-4}$; $\text{OR}_{\text{PF}} = 1.44$, 95% CI_{PF} : 1.11–1.85, P value $= 5.51 \times 10^{-4}$). Detailed results of the MR sensitivity check are presented in Supplementary Fig. 21 and Supplementary Data 31.

To assess potential collider bias introduced by BMI adjustment in the GWAS for BMFF, we additionally performed MR analyses using BMI-unadjusted BMFF GWAS summary statistics. Results were consistent with the primary analysis (Supplementary Data 32, 33), suggesting minimal bias from this source. In addition, we repeated MR analysis using an alternative osteoporosis GWAS summary statistics yielded consistent directional estimates, though with slightly attenuated effect sizes ($\text{OR}_{\text{LPF}} = 1.27$, 95% CI_{LPF} : 1.09–1.47, P value $= 1.99 \times 10^{-4}$; $\text{OR}_{\text{RPF}} = 1.26$, 95% CI_{RPF} : 1.06–1.49, P value $= 8.43 \times 10^{-4}$; $\text{OR}_{\text{PF}} = 1.27$, 95% CI_{PF} : 1.09–1.48, P value $= 1.65 \times 10^{-4}$; Supplementary Data 34, 35), supporting the robustness of our primary findings.

To address potential bias due to sample overlap between the exposure (BMFF GWAS) and outcome (osteoporosis GWAS) datasets,

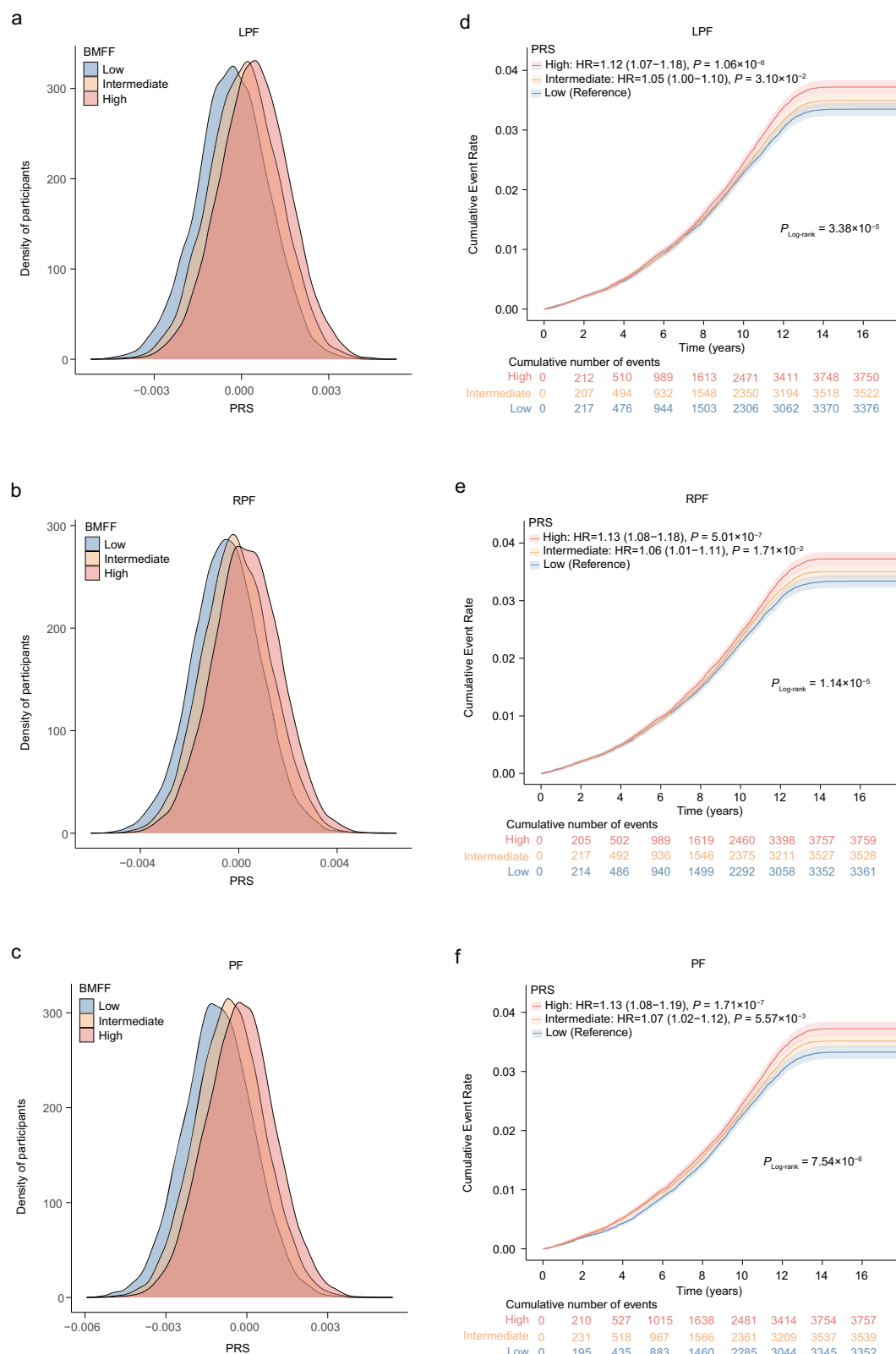


Fig. 5 | Distribution of PRS and cumulative osteoporosis incidence stratified by PRS. a–c Density plots show the distribution of PRS for participants with low, intermediate, and high BMFF that was defined based on the tertiles of normalized BMFF. PRS of left proximal femur (a), right proximal femur (b) and proximal femur (c) BMFF yielded discrimination for BMFFs. **d–f** Cox hazard proportional regression was utilized to compare osteoporosis incidence rates between low, intermediate, and high PRS groups with adjustment for age, sex, and BMI. Disease outcomes were identified based on ICD9 and ICD10. Strata based on PRS of left proximal femur (d),

right proximal femur (e), and proximal femur (f) BMFF. Those in the first tertiles of PRS are depicted in blue, the second tertiles are depicted in orange, and the last tertiles are depicted in red. The darker shades represent the central estimate of the cumulative incidence (defined as the Kaplan–Meier survival estimate). The lighter shades represent the respective 95% CIs. The x-axis depicts years since enrollment in the UKB; the y-axis depicts cumulative incidence. BMFF bone marrow fat fraction, PF proximal femur, LPF left proximal femur, RPF right proximal femur, PRS polygenic risk score, HR hazard ratio, CIs confidence intervals.

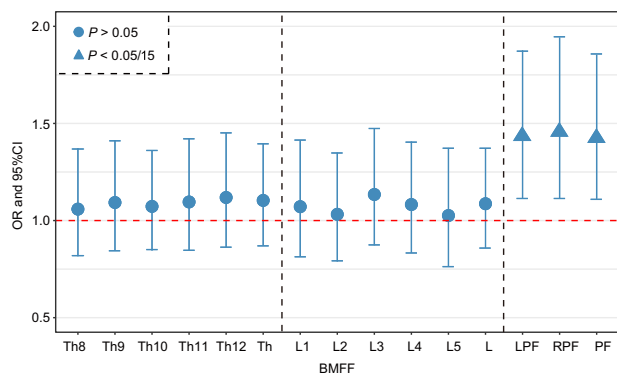


Fig. 6 | Causal effects between BMFF and osteoporosis using Mendelian randomization. The forest plots show the causal effects of BMFFs on osteoporosis. Disease outcomes were identified based on ICD9 and ICD10. The measure of center refers to causal effect sizes of BMFFs on osteoporosis, which are presented as ORs per standard deviation increment, with shape indicating significance levels: triangle denotes Bonferroni correction for significance (two-sided P value < 0.003 (0.05 divided by three principal components and five MR methods)) and round indicates non-significant correlations. The error bars represent 95% confidence intervals (95% CIs). MR analyses were performed using the R package TwoSampleMR with the inverse-variance weighted technique as our major model. The number of instrumental variables used was provided in Supplementary Data 30. The exact P values were provided in Supplementary Data 30. BMFF bone marrow fat fraction, Th thoracic vertebra, L lumbar vertebra, PF proximal femur, LPF left proximal femur, RPF right proximal femur, OR odds ratio, CIs confidence intervals.

we conducted two complementary analyses. First, since the osteoporosis GWAS was derived from the UKB study, but individual-level sample IDs were unavailable, we assumed potential sample overlap and applied MRlap¹⁷, a method that corrects for bias induced by overlapping samples. The corrected effect estimates showed no statistically significant difference compared to the observed estimates (P -difference > 0.05 ; Supplementary Data 36), suggesting minimal bias from overlap. Second, to definitively rule out overlap bias, we performed a non-overlapping GWAS for osteoporosis by excluding all individuals included in our BMFF GWAS from the UKB cohort. MR analysis using this independent osteoporosis GWAS yielded effect estimates consistent in direction with the original results, though slightly attenuated in magnitude ($OR_{LPF} = 1.20$, 95%CI_{LPF}: 1.06–1.35, P value = 3.76×10^{-4} ; $OR_{RPF} = 1.24$, 95%CI_{RPF}: 1.08–1.42, P value = 2.55×10^{-4} ; $OR_{PF} = 1.20$, 95%CI_{PF}: 1.07–1.36, P value = 2.91×10^{-4} ; Supplementary Data 37, 38). This consistency across analyses supports the robustness of our primary findings against sample overlap bias.

Furthermore, to investigate the reverse causality, we performed Mendelian randomization of BMD on BMFF. The result shows that there was a negative causal effect with the OR of 0.68–0.69 for proximal femur BMFF and 0.80–0.86 for vertebral BMFF (Supplementary Data 39, 40). These results, together with previous genetic correlation and PRS analyses, strengthen the evidence for a causal relationship between BMFF and osteoporosis.

Discussion

This study, as a large individual-level GWAS, investigated the genetic architecture of BMFF and provided biological insights into the relationship between BMFF and disease. We utilized a deep learning model to calculate 15 BMFFs of more than 38,000 individuals, with which GWASs identified 373 significant BMFF-associated variants. Pathway enrichment analyses indicated that mapped candidate genes are involved in bone development and remodeling, glucose and lipid metabolism and hematopoietic pathways. Genetic correlation analysis identified diseases, especially osteoporosis and fractures, associated with BMFF. Notably, we found that higher PRS of proximal femur

BMFFs was associated with an increased incidence of osteoporosis. Furthermore, Mendelian randomization verified the potential causation between proximal femur BMFF and osteoporosis (Fig. 7).

The IBAS-FFCS effectively achieves large-scale automatic quantification of BMAT and solves the limitation of quantitative methods, especially the dependence on manual image segmentation. Compared with manual segmentation and calculation, the consistency rate was more than 0.95, indicating that the performance of IBAS-FFCS is comparable to that of radiologists. A sample size of more than 38,000 would provide $>99\%$ statistical power ($\alpha = 5 \times 10^{-9}$) to detect common variants influencing BMFF with a SNP-based heritability of ~ 0.2 .

As the first step of data analysis, candidate variances ranging from 5116 to 7838 were identified by GWAS, implying the existence of extensive genetic regulation of BMFF. Most of the variants were located in the intronic and intergenic regions, suggesting their potential indirect roles in modulating gene expression as cis-regulatory elements. The enrichment in active histone markers, such as H3K4me1 and H3K4me3, also supported this opinion. Additionally, the enrichment of candidate variants within disease GWAS loci, such as osteoporosis, fracture, and anorexia nervosa, indicated that a similar genetic architecture may exist between BMFF and these diseases. This finding strengthens the growing evidence that the majority of GWAS risk variants influence disease risk via their regulatory activities.

Our GWAS identified similar genetic architectures across vertebral BMFF traits, suggesting common regulatory mechanisms. However, given variations in mechanical loading¹⁸ and endocrine influences^{19,20} across vertebral regions, analyzing individual vertebrae separately may be a viable approach for future studies to uncover site-specific genetic effects, although it would increase analytical costs. For femoral BMFF, we define the proximal femur as a combined region of the femoral head and total hip, which may provide insights into the overall role of BMFF in hip-related bone health. However, clinically, the femoral head is more relevant to conditions like osteoarthritis and osteonecrosis, while the total hip region is critical for fracture and osteoporosis risk. Moreover, previous studies have pointed out that there are differences in genetic structure between the femoral head and total hip¹⁴. This underscores the potential value of analyzing these subregions separately. Future research should prioritize high-resolution phenotyping to disentangle subregional BMFF contributions to distinct skeletal pathologies.

We identified several susceptibility genes by four strategies, some of which have been found to be involved in the maintenance of bone homeostasis and regulation of metabolic balance, such as *PPAR γ* ²¹, *LEPR*^{22,23}, *SBNO2*²⁴, *ALDH2*^{25,26}, *TBCID8*²⁷, *CHD7*²⁸, and *CCBE1*²⁹. For instance, a classical gene, *PPAR γ* , is a key regulator of adipocyte differentiation in the bone marrow. Overexpression of *PPAR γ* in bone marrow progenitor cells in transgenic mice leads to increased adipogenesis²¹. In contrast, inhibition of *PPAR γ* gene expression reduced bone marrow fat in mice, while increasing bone formation and osteoblast differentiation of bone marrow progenitors³⁰. For another example, the *LEPR*-encoded leptin receptor is indispensable for leptin action. The high expression of leptin receptor subtypes in bone marrow adipocytes and osteoblasts suggests a direct effect of leptin on bone metabolism^{22,23}. Peripheral administration of serum leptin showed that serum leptin increased bone formation and decreased bone resorption while inhibiting the adipogenic differentiation of bone marrow mesenchymal stromal cells^{31,32}, which was also confirmed in some in vitro studies^{33,34}. The results of pathway enrichment analysis reinforced that the candidate genes were significantly involved in bone and metabolic pathways, and the imbalance of these gene expressions may have an impact on the occurrence of bone-related and metabolic-related diseases. Additionally, we also found several genes involved in bone marrow hematopoiesis, such as *MLLT4*³⁵, *TERT*^{36,37}, *DUSP16*³⁸, and *CCBE1*²⁹. Pathway analysis also showed that candidate genes were enriched in hematopoietic pathways. This provides a clue to a

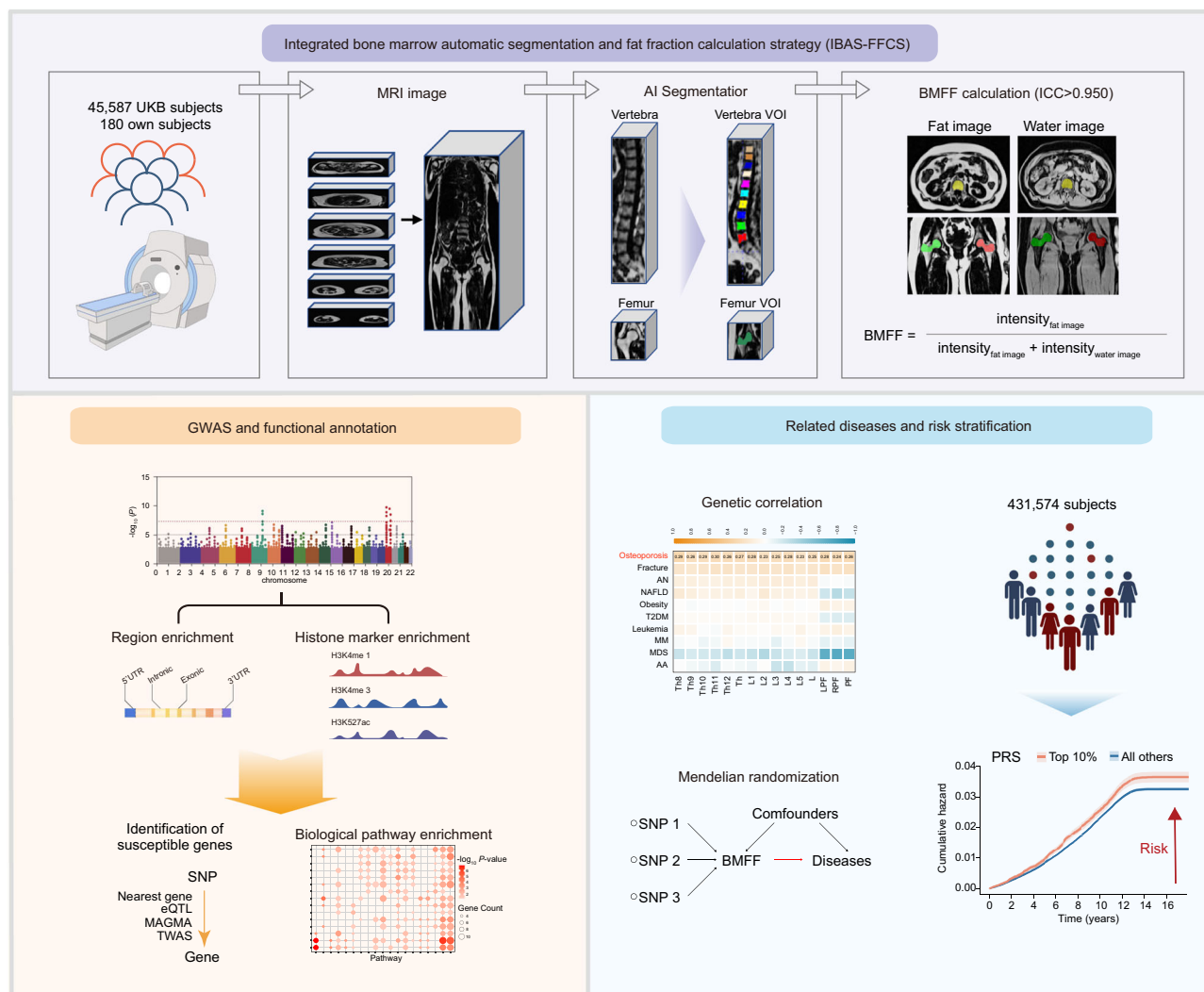


Fig. 7 | Genetic architecture of bone marrow fat fraction and its involvement in disease risk. Schematic workflow showing: (1) automated calculation of 15 BMFFs from MRI scans of 38,522 UK Biobank participants using our deep learning model; (2) genome-wide association studies identifying 373 significant BMFF-associated variants, and functional annotation revealed that BMFF is subject to extensive genetic regulation. (3) Genetic correlation analysis uncovered the relationships

between BMFF and skeletal diseases. Notably, polygenic risk scores for proximal femur BMFFs have a certain risk stratification ability for osteoporosis. Finally, Mendelian randomization confirms causal relationships between proximal femur BMFF and osteoporosis risk. Created in BioRender. Wu, Z. (2025) <https://BioRender.com/4c5yqdu>.

potential relationship between BMAT and hematopoiesis. Altogether, these results suggest that candidate genes may contribute to the development of skeletal, metabolic, and hematopoietic diseases.

A number of sex-specific BMFF-associated genes were identified. For instance, the male-specific gene *TERT* encodes telomerase, which plays a role in cellular senescence, as it is normally repressed in post-natal somatic cells, resulting in progressive shortening of telomeres. Diseases associated with *TERT* include pulmonary fibrosis and bone marrow failure syndrome³⁹, suggesting that *TERT* mutations may lead to bone marrow failure and thereby affect BMFF. Another male-specific gene, *CCDC91*, which is involved in bone remodeling and regulating osteogenesis, may indirectly affect BMFF production^{40,41}. A female-specific gene *JAZF1* is found at particularly high levels in adipose tissue and plays a role in lipid metabolism by suppressing lipogenesis, increasing lipolysis and decreasing lipid accumulation in adipose tissue⁴². It should be noted that *VMPI* was also reported as a female-specific gene in another BMFF study¹⁴. *VMPI* (vacuole membrane protein 1) functions as a phospholipid scramblase critical for lipid metabolism and cellular membrane remodeling, with emerging roles in autophagosome formation⁴³. Given that autophagy is a key regulator

of adipocyte differentiation and lipid droplet dynamics in white adipose tissue⁴⁴, the observed enrichment of *VMPI* expression in bone marrow stromal cells⁴⁵ suggests its potential involvement in modulating marrow adiposity through autophagy-dependent pathways. Compared to previous BMFF genetic studies¹⁴, we identified more sex-specific genes due to our multi-method approach, providing a more complete understanding of sex-specific BMFF regulation. Future investigations into sex-specific expression patterns of these candidate genes will be critical to elucidate the molecular mechanisms underlying sexual dimorphism in BMFF regulation.

Our estimated heritability of BMFF fluctuates around 0.20, implying that about 20% of BMFF variance is attributable to genetic factors. This estimate is slightly lower than the estimated heritability (0.31–0.36) of volumes of visceral adipose tissue, abdominal subcutaneous adipose tissue and gluteal adipose tissue from other study⁴⁶. The genetic correlation analysis among BMFF highlighted that genetic correlation within the same type of BMFF was large, while between different types of BMFF was relatively low. Some studies have also pointed out the differences between BMFF at different sites. For example, the BMAT at the proximal tibia and distal femur can easily

expand or deplete in response to a variety of stimuli, while the BMAT in the distal tibia and rodent caudal vertebrae appears early in life and remains relatively stable⁴⁷. Our results suggest that the reason for this difference is the discrepant genetic structure of BMFF.

We observed genetic correlations between BMFFs and multiple clinical measures, especially BMD, triglyceride (TG) and hemoglobin (Hb). Previous studies have reached the same conclusion at the phenotypic level. For example, Idoia Labayen et al. conducted a case-control study and found that lumbar BMFF was negatively correlated with lumbar BMD⁴⁸, as did several other studies^{49–51}. Apart from measures, we would like to explore the genetic correlation between BMFFs and clinical diseases. We discovered significant genetic correlations between BMFFs and osteoporosis and fractures, which is also supported by phenotypic studies. In a study including 50 postmenopausal women and 12 younger women as control subjects, proton density fat fraction (PDFF9) at the spine was significantly higher in osteoporosis patients compared to controls⁵². Other studies using bone biopsy to assess bone marrow fat have also reported associations with osteoporosis^{53,54}. Not surprisingly, some studies have also reported an association between higher BMFF and higher fracture risk^{53,55}. For example, in a case-control study, 26 women with vertebral fractures had higher BMFF than age-matched controls (P value = 0.02)⁵³. In addition, case-control studies and animal experiments have also concluded that there is a phenotypic association between BMFF and anorexia nervosa^{7,56}. These results suggest that genetic and phenotypic correlations complement each other to jointly demonstrate the relationship between BMFF and disease.

We constructed valid PRS for each BMFF and observed that proximal femur BMFF PRSs associate with osteoporosis risk, which also implies the hypothesis that BMFF is the etiology of osteoporosis. Notably, although the ability of BMFF PRS alone to predict osteoporosis risk may be unsatisfactory, surprising results may be achieved by optimizing the prediction by utilizing multiple PRS in the joint model based on a range of different traits such as BMD, serum calcium, estrogen, etc. At present, the predictive ability of PRS for disease has been gradually validated in other domains, such as chronic obstructive pulmonary disease⁵⁷ and cardiovascular diseases⁵⁸. How to develop PRS for BMFF and even more traits to enhance risk stratification for osteoporosis is a promising research direction in the future.

The results of Mendelian randomization were generally consistent with upstream analysis, upgrading the association to the causal link between BMFF and osteoporosis. Genetic correlation, PRS, and Mendelian randomization analyses all suggest a significant effect for proximal femur BMFF on osteoporosis. These findings provide credible evidence to support the hypothesis that BMFF exerts a causal influence on osteoporosis, which can be partially supported by previous researches. For instance, it has been proposed that BMAT can act as an endocrine/paracrine organ, affecting the homeostasis of osteoblasts and osteoclasts³⁹, which are key cells in the development of osteoporosis³. Specifically, marrow adipogenic lineage precursors (MALPs) express key osteoclast regulatory factors (including RANKL) at much higher levels than other mesenchymal cells in young and adult mice, which enhances bone resorption and leads to pathological bone loss⁶⁰. BMAT secretes adiponectin, which acts on receptors on osteoblasts, hamper their proliferation and favor their apoptosis, altogether decreasing bone mass⁶¹. These findings effectively support our results and contribute to the identification of BMFF as one of the etiologies of osteoporosis and fracture. Furthermore, our reverse Mendelian randomization analysis revealed a negative causal effect of BMD on BMFF, suggesting a bidirectional relationship between BMD and marrow adiposity. This reciprocal interaction underscores the complexity of bone metabolism, where changes in one component may influence the other, potentially through shared regulatory mechanisms. Further studies are needed to elucidate the underlying pathways driving this relationship. On the other hand, the occurrence of this causal

relationship may also be due to that high BMD may affect the determination of bone marrow fat fraction, thus producing falsely low bone marrow fraction. Given that our BMFF were generated using a two-point Dixon sequence, it should be noticed that measurement errors of roughly 3–5% may arise from B_0 inhomogeneity, T_1 weighting bias, uncorrected T_2 decay, the multi-peak spectral complexity of fat and partial-volume effects^{62–64}, particularly in individuals with high BMD. Consequently, although our Mendelian randomization analysis provides evidence for a causal effect of elevated BMD on reduced BMFF, these inherent imaging biases necessitate cautious interpretation of absolute BMFF values.

We acknowledge some limitations in our study. First, included participants were predominantly sourced from European populations, which constrains the broader applicability of our findings. In the future, the reliability of our results should be validated in more diverse and larger cohorts representing various ethnicities. Second, despite we randomly split the GWAS cohort into two subsets for pseudo-replication, a true replication of the GWAS is needed in the future to ensure that a genotype-phenotype association observed in the GWAS represents a credible association. Additionally, while PRSs derived from proximal femur BMFF showed associations with an increased risk of osteoporosis, it is important to recognize that the predictive performance of these PRSs were relatively limited. Our future research will focus on identifying additional genetic loci and molecular markers, with the goal of enhancing the predictive capabilities of our models. Lastly, although we identified numerous loci, genes and biological pathways related to BMFF and established connections to disease, the underlying mechanisms remain to be fully elucidated. Therefore, precise cell and animal experiments are needed in the future.

In conclusion, we utilized an advanced deep learning model capable of quantifying BMFF measured by whole-body MRI. We uncover a large number of significant variant-BMFF associations, and implicate candidate genes linked to skeletal, metabolic and hematopoietic systems. Moreover, we observe PRSs derived from proximal femur BMFFs are associated with incident osteoporosis, and Mendelian randomization suggests a causal relationship between BMFFs and osteoporosis. Altogether, these findings represent a substantial advance in our understanding of the genetic architecture of BMFF and shed light on the biological basis for osteoporosis etiology, which may lead to potential therapeutic targets and personalized risk stratification strategies in the future.

Methods

Ethics

The research reported herein was done in compliance with all ethical requirements. Data for the present study were obtained under an approved UKB project application (ID 94939), which provided specific approval to measure BMFF from the UKB MRI data. UKB has ethics approval from the National Health Service North-West Center Research Ethics Committee (Ref11/NW/0382). All UKB participants provided their consent to take part in the UKB study. The UKB is conducted in accordance with criteria set by the Declaration of Helsinki, with participants providing informed written consent to take part and to be followed up through national record linkage. Our own independent external validation data were derived from a prospective cohort, which was approved by the Institutional Review Board of Tongji Hospital Affiliated to Tongji Medical College of Huazhong University of Science and Technology (Approved No. of ethic committee: TJ-IRB20231272; Registration number: ChiCTR2400085853).

Study population

UKB is a large prospective cohort study that recruited more than 500,000 participants aged 40–69 between 2006 and 2010. At baseline, comprehensive information on the participants was collected, including demographic information, anthropometric measurements,

biological samples, lifestyle, as well as genotype data and imaging data necessary for this study. More detailed information about UKB have been released⁶⁵.

Semantic segmentation and deep learning model training

Imaging data in UKB. The Dual-echo Dixon Vibe protocol of UKB were acquired from a Siemens Aera 1.5T MRI scanner (Magnetom Aera, Siemens Medical Solutions, Erlangen, Germany). This scanning protocol consists of six independent sequences, covering the region from the neck to the knees. Key scanning parameters include: TR/TE in-phase 6.7/4.8 ms, TR/TE out-phase 6.7/2.4 ms, slice thickness 3.5/4.5 mm, field of view (FOV): 500 × 381 mm. For more detailed scanning parameters, please refer to this ref. ⁶⁶.

Model design and workflow. The study developed an integrated bone marrow automatic segmentation and fat fraction calculation strategy (IBAS-FFCS). We used ten vertebrae (the eighth thoracic vertebra to the fifth lumbar vertebra) and the proximal femurs on both sides to evaluate BMFF. The proximal femur consists of the femoral head, femoral neck, and trochanter; the lower boundary was defined as the inferior tip of the greater trochanter. The whole-body MRI imaging is not a continuous volume but is instead provided as six different sequences, with overlapping images between adjacent sequences. First, the Dixon data were preprocessed and fused into a unified 3D image using an automated fat-water swap detection and correction program⁶⁷, with publicly available preprocessing code accessible at <https://github.com/recoh/pipeline>. Then, spatial normalization was conducted by resampling the MRI images into 2.23 × 2.23 × 3 mm.

Following preprocessing of the data, three radiologists with more than 5 years of clinical experience manually outlined volumes of interest (VOIs) on the native axial fat images using ITK-SANP (version 4.0.1) as the reference standard. To reduce delineation discrepancies among observers, the three radiologists underwent training to ensure consistent outlining, with a focus on avoiding cortical bone edges and maximizing the inclusion of bone marrow tissue. To ensure the accuracy of the study, each radiologist was asked to draw the same set of 30 cases and assess the consistency among observers. Moreover, the accuracy of all VOIs was validated through visual inspection by seasoned experts before their integration into the modeling procedure. For training and validating the segmentation model, a random sample of 406 subjects for the spine and 257 subjects for the proximal femur were extracted from the UKB database and manually segmented.

The 3D-Unet architecture was employed for the segmentation algorithm of the vertebra and proximal femur. A fixed crop was applied with patch sizes of 96 × 96 × 256 for the spine and 128 × 96 × 128 for the femur to serve as inputs for the segmentation models. Notably, femur cropping is automated through a fixed, predefined subvolume extraction using the region [46:174, 40:104, 201:329] (x, y, z). This standardized subvolume reliably captures the complete proximal femur region from the whole-body volume, ensuring consistency across all subjects. Additionally, data augmentation included scaling intensity, random flipping, random Gaussian noise, and automatic contrast adjustment were conducted. The model development involved a basic structure comprising 3D Convolutional Layers, Leaky ReLU activation, and Batch Normalization, with network initialization following the Kaiming normal distribution. Four stages in encoding and decoding counterparts indicate that four-level scales of feature maps were formulated for automatic feature extraction. In the encoding part, each stage consists of two convolutional layers with a 3 × 3 × 3 kernel and a max pooling layer with a 2 × 2 × 2 kernel and a 2 × 2 × 2 stride to compress spatial information; In the decoding part, each stage consists of two convolutional layers with 3 × 3 × 3 kernel and a transpose convolutional layer with 3 × 3 × 3 kernel and 2 × 2 × 2 stride for spine and femur reconstruction. For training this segmentation model, the Dice loss function was utilized for optimization. The model parameters were updated using the Adam Optimizer, with a weight

decay of 10⁻⁵ and beta values of 0.900–0.999. A cosine annealing learning rate decay method was applied, starting with an initial learning rate of 10⁻³ and running for a maximum of 250 epochs.

MR-based BMFF measurements. The dual-echo Dixon method is a widely used MRI technique to quantify fat fraction (FF) in tissues. The dual-echo Dixon method utilizes the distinct resonant frequencies of hydrogen atoms in fat and water molecules to separate and quantify their respective signals in MRI imaging. Based on the intensities of water and fat images, BMFF was measured using Eq. (1)^{68,69}:

$$\text{BMFF} = \frac{\text{intensity}_{\text{fatimage}}}{\text{intensity}_{\text{fatimage}} + \text{intensity}_{\text{waterimage}}} \quad (1)$$

The VOIs of vertebra and proximal femur segmented using our deep learning models, was eroded by a single boundary voxel in plane to ensure measurements were exclusively obtained from cancellous bone, but no cortical bone, before extracting the BMFF for each VOI. BMFF is calculated based on the stitched original images.

GWAS sample selection

The procedure for GWAS sample inclusion and exclusion is shown in Supplementary Fig. 2. From an initial pool of 51,487 UK Biobank participants with whole-body MRI data, we applied sequential exclusions for: (1) missing genotypes, (2) non-White population based on UKB field 22006, (3) BMI <16 or >40 kg/m², (4) Zero or missing BMFF data due to the segmentation error (Supplementary Fig. 1), (5) extreme BMFF values (<Q1 - 3 × IQR or >Q3 + 3 × IQR), and (6) individuals with relatedness based on family relatedness derived by UKB (One individual from each cluster of related individuals was retained based on data availability). Finally, participants ranging from 38,522 to 39,178 were included in the GWAS.

Genotyping and imputation

The genotyping process and DNA arrays used in the UKB study have been described in more detail elsewhere⁶⁵. In brief, participants were genotyped by Affymetrix using the Applied Biosystems UK BiLEVE Axiom Array (807,411 markers tested for 49,950 participants) or Applied Biosystems UKB Axiom Array (825,927 markers tested for 438,427 participants). More than 95% of the single-nucleotide polymorphisms (SNPs) tested are shared between these arrays. On the basis of merged UK10K and 1000 Genomes phase 3 panels, IMPUTE3 and SHAPEIT3 were used for imputation. Variant positions refer to the GRCh37/hg19 human genome.

Genome-wide association study

We computed residuals for each BMFF by regressing them on covariates such as age at the imaging assessment, sex, and BMI at the imaging assessment. Subsequently, after rank-based inverse normal transformation of these residuals, we performed GWAS for the 15 transformed BMFFs using BOLT-LMM v2.3.6⁷⁰. This analysis utilized ~8.5 million well-imputed variants, each with a minor allele frequency (MAF) of ≥1%, a deletion rate ≤0.05, Hardy–Weinberg *P* value ≥1 × 10⁻⁶ and an imputation quality (INFO) score >0.4. GWAS analysis models were adjusted for age at the imaging assessment, sex, BMI at the imaging assessment, and PC 1–10. BOLT-LMM accounts for ancestral heterogeneity, cryptic population structure, and sample relatedness by fitting a linear mixed model with a Bayesian mixture prior as a random effect^{71–73}. The genomic inflation factor ranged from 1.011 to 1.014, and the LDSC intercept consistently ranged from 1.0011 to 1.0019¹⁶ (Supplementary Fig. 10). This indicates that the BMFF traits were influenced more by polygenicity than by population structure. GWAS power was calculated using GCTA package (<https://yanglab.westlake.edu.cn/software/gcta/#GREMLpowercalculator>), resulting >99% statistical power ($\alpha = 5 \times 10^{-9}$). To identify genetic loci, we uploaded this summary statistic to the FUMA platform v1.5.0¹⁵. Using the 1000GPhase3 EUR as a

reference panel, we identified independent significant variants at the statistical significance threshold P value $<5 \times 10^{-9}$. This threshold was determined using a conservative Bonferroni correction, in which 0.05 was divided by the total number of SNPs analyzed in our GWAS (8,412,349), yielding $\sim 5 \times 10^{-9}$. All variants at $r^2 < 0.1$ with each other were considered as independent significant variants, and a fraction of the independent significant variants in approximate linkage equilibrium with each other at $r^2 < 0.05$ were considered as lead variants.

To check the robustness of our GWAS results, we performed three sensitivity check analyses, including a (1) sex-stratified GWAS for male and female based on biological sex, (2) split-sample GWAS by randomly dividing the entire population into two splits at a 7:3 ratio (sex and age matched), and (3) GWAS without BMI adjustment. For each analysis, we compared the effect sizes (β coefficients) of lead variants between subgroups (e.g., men vs. women, split 1 vs. split 2) using Pearson correlation analysis and two-sample t -tests to evaluate their consistency. We also analyzed the Sex \times genotype interaction to calculate t -sex and P sex developed by ref. 74.

Gene mappings

We utilized four approaches to map genome-wide significant loci to genes, the first three of which were through FUMA default settings and specialized datasets, as described as follows: (1) physical positional mapping assigns the lead variant to its physically nearest genes within a 10-kB window in the human reference assembly (GRCh37/hg19). (2) eQTL mapping found genes whose expression levels are associated with variants, where we considered eQTLs within adipose subcutaneous, adipose visceral omentum and whole blood from GTEx v8. P value <0.05 was considered statistically significant. (3) MAGMA⁷⁵ mapping conducted a generalized gene-based analysis including 18,887 protein-coding genes. Variants within exonic, intronic, and untranslated regions were chosen for each gene. The mean of the summary statistic (χ^2) of GWAS for the variants in a gene was used to determine the gene-based P value. Bonferroni correction determined 2.65×10^{-6} (0.05/18887) as the threshold for significance. The above three analyses were performed by FUMA. (4) TWAS identified the most strongly associated gene at each locus based on imputed cis-regulated gene expression by FUSION⁷⁶. Pre-computed predictive models of GTEx v8 multi-tissue expression (adipose subcutaneous, adipose visceral, and muscle skeletal) were downloaded from the FUSION website (<http://gusevlab.org/projects/fusion/>). Bonferroni correction determined 0.05 divided by the number of genes as the threshold for significance, resulting in 5.13×10^{-6} (0.05/9752), 6.41×10^{-6} (0.05/7796), and 5.87×10^{-6} (0.05/8515) for adipose subcutaneous, adipose visceral, and muscle skeletal, respectively.

Functional annotations of susceptible genes

The genes identified by the four strategies were pooled as susceptible genes. Gene Ontology (GO)⁷⁷ term enrichment analyses in biological process was performed for these susceptible genes using an online tool Metascape⁷⁸ (<https://metascape.org/>). We defined a P value <0.05 as statistically significant. Tissue-specific gene expression analysis were performed by MAGMA gene-set analysis, which was integrated in FUMA. This analysis examines whether the expression of susceptible genes in a given tissue is higher than the average expression across all tissues. We reported the results from the 54 tissue types using the GTEx v8 data. FDR <0.05 was considered statistically significant.

Colocalization

We performed colocalization analyses between BMFF GWAS and eQTL data. Common variants from our BMFF GWAS were integrated with eQTL summary statistics derived from gene expression references in mesodermal tissues (subcutaneous adipose tissue, visceral omentum adipose tissue, and skeletal muscle tissue) and lymphoid tissues

(spleen tissue and Epstein-Barr virus [EBV]-transformed lymphocytes) obtained from GTEx v8. The colocalization analysis evaluated five hypotheses: H0 (no association), H1 (GWAS association only), H2 (eQTL association only), H3 (both associations without colocalization), and H4 (both associations with colocalization). The posterior probability of hypothesis 4 (PPH4) quantifies the likelihood that a locus is colocalized due to a single causal variant, as opposed to two distinct causal variants (PPH3). Loci with PPH4 $>80\%$ were considered significantly colocalized. Independent significant variants were mapped to genes using the variant effect predictor⁷⁹, and colocalization analyses were conducted using the coloc.abf function from the Coloc R package⁸⁰.

Heritability and genetic correlation

Previous literature demonstrates that BMFF, as a unique adipose tissue, is associated with bone-related disorders (e.g., osteoporosis) and metabolic diseases (e.g., diabetes and obesity)^{59,81}. Additionally, given its location within the bone marrow, BMFF has potential links to the hematopoietic system^{2,82}. Therefore, we focused on 13 clinical measures related to the skeletal, metabolic, and hematopoietic systems, including bone mineral density⁸³, oestradiol⁸⁴, calcium⁸⁴, glucose⁸⁴, triglycerides⁸⁴, high density lipoprotein cholesterol⁸⁴, low density lipoprotein cholesterol⁸⁴, body mass index⁸⁵, hemoglobin concentration⁸⁴, white blood cell count⁸⁶, platelet count⁸⁴, red blood cell count⁸⁴ and reticulocyte count⁸⁴, as well as ten diseases including osteoporosis⁸⁷, fracture⁸³, anorexia nervosa⁸⁸, nonalcoholic fatty liver disease⁸⁹, obesity⁹⁰, type 2 diabetes⁹¹, leukemia⁹², multiple myeloma⁹⁰, myelodysplastic syndrome⁹⁰, and aplastic anemia⁹³, to comprehensively investigate the clinical relevance of BMFF.

LDSC¹⁶ software was used to estimate the heritability of 15 BMFFs and to evaluate genetic correlation (1) between 15 BMFFs; (2) between BMFFs and 13 related clinical measures; (3) between BMFFs and ten related diseases. Data sources of summary statistics for genetic correlation analyses were listed in Supplementary Data 24. These analyses were performed according to the standard analysis process of LDSC. We performed LDSC using well-imputed HapMap3 variants (http://ldsc.broadinstitute.org/static/media/w_hm3.noMHC.snplist.zip) and pre-computed LD scores of European ancestry from the 1000 Genomes Project Phase 3 (https://data.broadinstitute.org/alkesgroup/LDSCORE/eur_w_ld_chr.tar.bz2). We did not constrain the intercepts in LDSC analysis, which could not only account for residual confounding but also indicate whether there was potential sample overlap between the two GWAS studies. P value $<1.28 \times 10^{-3}$ (0.05 divided by 13 clinical measures and three principal components) was considered statistically significant for analysis between BMFFs and measures. P value $<1.67 \times 10^{-3}$ (0.05 divided by 10 clinical diseases and 3 principal components) was considered statistically significant for analysis between BMFFs and diseases.

Polygenic risk score

We adopted the C + T (clumping + thresholding) strategy⁹⁴ to construct PRS of each BMFF based on Eq. (2)

$$\text{PRS} = \sum_{i=1}^n \beta_i \text{SNP}_i \quad (2)$$

where n means the number of variants, SNP_i (0, 1, or 2) means the number of risk alleles for the i th variant, and β_i means the effect size of the risk alleles from BMFF GWASs. As shown in Supplementary Fig. 22, for SNP QC in PRS, in addition to the GWAS QC criteria, we further removed ambiguous SNP, multi-allelic SNP, and SNP previously reported to be associated with the corresponding diseases ($P < 5 \times 10^{-8}$ in the GWAS catalog (<https://www.ebi.ac.uk/gwas/home>)). We then applied clumping using PLINK with the following parameters: `--clump-kb 250`, `--clump-p1 1e-5`, `--clump-p2 5e-2`, and `--clump-r2 0.1`. For sample QC, we

selected all participants available in the UKB (502,379), excluding (1) participants lacking genotype data, (2) participants who do not meet QC for genetic data based on UKB Data field 22020, (3) non-White participants based on UKB field 22006, (4) participants who have withdrawn from UKB, and (5) already included in the GWAS, finally leaving 303,911 individuals. Next, for each disease cohort, we excluded individuals who had the corresponding disease before baseline, in accordance with the principles of cohort study⁹⁵. We repeated this procedure for each of the 15 BMFFs, producing 15 PRSs.

Normality tests showed that PRSs conformed to a normal distribution. We categorized participants into three PRS groups: low (lowest tertile), intermediate (second tertile) and high (highest tertile). To evaluate the association between BMFF PRS and disease incidence rates, Cox hazard proportional regression was utilized to compare disease incidence rates between the three PRS groups with adjustment for age, sex and BMI. P value $<1.67 \times 10^{-3}$ (0.05 divided by 10 clinical diseases and 3 principal components) was considered statistically significant. ROC and calibration plot were generated, and the AUC, C-statistic, AIC, BIC, R^2 , NRI, and IDI was calculated to evaluate the discriminative ability of PRS on osteoporosis. DeLong's test was employed to compare the differences in the AUC. We tested three predictive models: (1) adjusting clinical risk factors, including age, sex, BMI, and BMD; (2) adjusting PRS; (3) adjusting clinical risk factors and PRS.

Mendelian randomization

Two-sample Mendelian randomization was used to explore the causal effects of 15 BMFFs on osteoporosis. The clump command of PLINK v.1.9 was used to select the instrumental variables for each BMFF with parameters of P value $<5 \times 10^{-8}$, $r^2 < 0.001$, and kb = 10. SNPs within highly pleiotropic regions, the MHC region (hg19 coordinates: Chromosome 6, 28,477,797–33,448,354 base pairs) was excluded. In addition, we not only excluded SNPs that were directly associated with osteoporosis or BMD but also any SNPs with LD proxies ($r^2 \geq 0.6$) that were associated with osteoporosis or BMD ($P < 5 \times 10^{-8}$ in the GWAS catalog (<https://www.ebi.ac.uk/gwas/home>)). The osteoporosis GWAS summary files were selected based on the largest sample size GWAS study with a harmonized genome build (hg19) and standard QC criteria conducted in the White population currently available⁹⁰. The MR main program uses the R package TwoSampleMR⁹⁶, which by default conducts five different MR methods, including Egger, weighted median, simple mode, weighted mode estimators, and IVW. The most widely used IVW is considered our main method. Cochran's Q was computed to quantify heterogeneity across the individual causal effects, with a $P < 0.05$ indicating the presence of heterogeneity, and that consequently, random-effects IVW models are applied; otherwise, the fixed-effect IVW models are applied^{97,98}. To determine whether any discernible influence was mediated by outliers, the MR Pleiotropy RESidual Sum and Outlier (MR-PRESSO)⁹⁹. P value <0.003 (0.05 divided by 3 principal components and 5 MR methods) was considered statistically significant. The MR sensitivity analyses were conducted to test heterogeneity (Cochran's Q test), pleiotropy (MR-PRESSO), and F-statistics. In addition, scatter plot, funnel plot, forest plot, and leave-one-out analyses were drawn.

To support the robustness of our primary findings, we performed two repeated MR analysis (1) using BMI-unadjusted BMFF GWAS summary statistics, and (2) using an alternative osteoporosis GWAS summary statistic¹⁰⁰. To address potential bias due to sample overlap between the exposure (BMFF GWAS) and outcome (osteoporosis GWAS) datasets, we conducted two complementary analyses: (1) correcting causal effects estimate using MRlap¹⁷, a robust method that corrects for bias induced by overlapping samples in two-sample MR; (2) performing a non-overlapping GWAS for osteoporosis as outcome GWAS of MR analysis by excluding all individuals included in our BMFF GWAS from the UKB cohort. This GWAS analysis utilized

~8.5 million variants, each with MAF of $\geq 1\%$, deletion rate ≤ 0.05 , Hardy–Weinberg P value $\geq 1 \times 10^{-6}$ and INFO score >0.4 . For sample QC, from an initial pool of UKB participants, we applied sequential exclusions for: (1) missing genotypes, (2) non-White population based on UKB field 22006, (3) participants who have withdrawn from UKB, (4) already included in the BMFF GWAS, and (5) individuals with relatedness based on family relatedness derived by UKB, finally leaving 306,415 individuals (12,033 cases) as the osteoporosis GWAS sample. The outcome of osteoporosis was defined and coded in the ninth and tenth edition of the International Classification of Diseases (ICD9 and ICD10) (Supplementary Data 42). This GWAS was conducted using PLINK v.1.9 logistic model adjusted for age, sex, BMI, and PC 1–10.

To investigate the reverse causality, we performed MR of BMD^{101,102} on BMFF. The process of the instrumental variable selection was the same as above. In addition, we not only excluded SNPs that were directly associated with osteoporosis ($P < 5 \times 10^{-8}$ in the GWAS catalog) or BMFF (independent significant SNPs) but also any SNPs with LD proxies ($r^2 \geq 0.6$) that were associated with osteoporosis or BMFF.

Covariates and disease definitions

The outcome of disease was defined and coded in the ICD9 and ICD10. The UKB Data Fields of covariates and diseases were listed in Supplementary Data 41, 42.

Additional and detailed analyses are available in the Supplementary Methods.

Reporting summary

Further information on research design is available in the Nature Portfolio Reporting Summary linked to this article.

Data availability

Data from the UKB are available to all researchers upon making an application. This research has been conducted using the UKB Resource under Application no. 94939. All data for BMFF and BM segmentation volumes have been deposited in the UKB (upload ID 6693), where they will be available to any individuals with an approved UKB project. Data sources of publicly available GWAS results were listed in Supplementary Data 24. The GWAS summary statistics generated in this study have been deposited in the Human Genome Research Institute GWAS Catalog (<https://www.ebi.ac.uk/gwas/home>) under accession codes: GCST90652380 to GCST90652394 for the 15 BMFF.

Code availability

The code for deep learning-based segmentation of bone marrow volumes is publicly available on the GitHub repository 1295433015/IBAS-FFCS_project at https://github.com/1295433015/IBAS-FFCS_project¹⁰³ under the Apache-2.0 license and on Zenodo under <https://doi.org/10.5281/zenodo.16519540>. Users may reuse, modify, and distribute the code in accordance with the license terms, with appropriate attribution to the original authors. Aside from this, other bioinformatics and statistical analysis tools used in the present study are open source, and details about them can be found in the Methods section.

References

- Wang, Y. et al. Bone marrow adipocyte: Origin, biology and relationship with hematological malignancy. *Int. J. Lab Hematol.* **46**, 10–19 (2024).
- Wang, H., Leng, Y. & Gong, Y. Bone marrow fat and hematopoiesis. *Front. Endocrinol.* **9**, 694 (2018).
- Manolagas, S. C. Birth and death of bone cells: basic regulatory mechanisms and implications for the pathogenesis and treatment of osteoporosis. *Endocr. Rev.* **21**, 115–137 (2000).

4. Sheu, Y. et al. Vertebral bone marrow fat, bone mineral density and diabetes: the osteoporotic fractures in men (MrOS) study. *Bone* **97**, 299–305 (2017).
5. Zhu, L. et al. Marrow adiposity as an indicator for insulin resistance in postmenopausal women with newly diagnosed type 2 diabetes - an investigation by chemical shift-encoded water-fat MRI. *Eur. J. Radiol.* **113**, 158–164 (2019).
6. Vander Wyst, K. B. et al. Bone marrow adipose tissue content in Latino adolescents with prediabetes and obesity. *Obesity* **29**, 2100–2107 (2021).
7. Bredella, M. A. et al. Increased bone marrow fat in anorexia nervosa. *J. Clin. Endocrinol. Metab.* **94**, 2129–2136 (2009).
8. Mattiucci, D. et al. Bone marrow adipocytes support hematopoietic stem cell survival. *J. Cell Physiol.* **233**, 1500–1511 (2018).
9. Zhou, B. O. et al. Bone marrow adipocytes promote the regeneration of stem cells and haematopoiesis by secreting SCF. *Nat. Cell Biol.* **19**, 891–903 (2017).
10. Tratwal, J. et al. Reporting guidelines, review of methodological standards, and challenges toward harmonization in bone marrow adiposity research. Report of the methodologies working group of the international bone marrow adiposity society. *Front Endocrinol.* **11**, 65 (2020).
11. Singhal, V. & Bredella, M. A. Marrow adipose tissue imaging in humans. *Bone* **118**, 69–76 (2019).
12. Sollmann, N. et al. MRI-based quantitative osteoporosis imaging at the spine and femur. *J. Magn. Reson. Imaging* **54**, 12–35 (2021).
13. Morris, D. M. et al. A novel deep learning method for large-scale analysis of bone marrow adiposity using UK Biobank Dixon MRI data. *Comput. Struct. Biotechnol. J.* **24**, 89–104 (2024).
14. Xu, W. et al. Deep learning and genome-wide association meta-analyses of bone marrow adiposity in the UK Biobank. *Nat. Commun.* **16**, 99 (2025).
15. Watanabe, K., Taskesen, E., van Bochoven, A. & Posthuma, D. Functional mapping and annotation of genetic associations with FUMA. *Nat. Commun.* **8**, 1826 (2017).
16. Bulik-Sullivan, B. K. et al. LD Score regression distinguishes confounding from polygenicity in genome-wide association studies. *Nat. Genet.* **47**, 291–295 (2015).
17. Mounier, N. & Kutalik, Z. Bias correction for inverse variance weighting Mendelian randomization. *Genet. Epidemiol.* **47**, 314–331 (2023).
18. Ignasiak, D., Rüeger, A., Sperr, R. & Ferguson, S. J. Thoracolumbar spine loading associated with kinematics of the young and the elderly during activities of daily living. *J. Biomech.* **70**, 175–184 (2018).
19. Jia, L. & Cheng, M. Correlation analysis between risk factors, BMD and serum osteocalcin, CatheK, PINP, β -crosslaps, TRAP, lipid metabolism and BMI in 128 patients with postmenopausal osteoporotic fractures. *Eur. Rev. Med. Pharm. Sci.* **26**, 7955–7959 (2022).
20. Ojala, R. et al. Bone marrow metabolism is impaired in insulin resistance and improves after exercise training. *J. Clin. Endocrinol. Metab.* **105**, e4290–e4303 (2020).
21. Cock, T. A. et al. Enhanced bone formation in lipodystrophic PPARgamma(hyp/hyp) mice relocates haematopoiesis to the spleen. *EMBO Rep.* **5**, 1007–1012 (2004).
22. Iwamoto, I., Fujino, T. & Douchi, T. The leptin receptor in human osteoblasts and the direct effect of leptin on bone metabolism. *Gynecol. Endocrinol.* **19**, 97–104 (2004).
23. Kapur, S. et al. Leptin receptor (Lepr) is a negative modulator of bone mechanosensitivity and genetic variations in Lepr may contribute to the differential osteogenic response to mechanical stimulation in the C57BL/6J and C3H/HeJ pair of mouse strains. *J. Biol. Chem.* **285**, 37607–37618 (2010).
24. Li, T. et al. Gender-specific SBNO2 and VPS13B as a potential driver of osteoporosis development in male ankylosing spondylitis. *Osteoporos. Int.* **32**, 311–320 (2021).
25. Malkovskiy, A. V. et al. The effect of ethanol consumption on composition and morphology of femur cortical bone in wild-type and ALDH2*2-homozygous mice. *Calcif. Tissue Int.* **108**, 265–276 (2021).
26. Tsuchiya, T. et al. Disruption of aldehyde dehydrogenase 2 gene results in altered cortical bone structure and increased cortical bone mineral density in the femoral diaphysis of mice. *Bone* **53**, 358–368 (2013).
27. Hsu, Y. H. et al. An integration of genome-wide association study and gene expression profiling to prioritize the discovery of novel susceptibility Loci for osteoporosis-related traits. *PLoS Genet.* **6**, e1000977 (2010).
28. Liu, C. et al. CHD7 regulates bone-fat balance by suppressing PPAR- γ signaling. *Nat. Commun.* **13**, 1989 (2022).
29. Weivoda, M. M. et al. Identification of osteoclast-osteoblast coupling factors in humans reveals links between bone and energy metabolism. *Nat. Commun.* **11**, 87 (2020).
30. Akune, T. et al. PPARgamma insufficiency enhances osteogenesis through osteoblast formation from bone marrow progenitors. *J. Clin. Invest.* **113**, 846–855 (2004).
31. Cornish, J. et al. Leptin directly regulates bone cell function in vitro and reduces bone fragility in vivo. *J. Endocrinol.* **175**, 405–415 (2002).
32. Turner, R. T. et al. Peripheral leptin regulates bone formation. *J. Bone Min. Res.* **28**, 22–34 (2013).
33. Motyl, K. J. & Rosen, C. J. Understanding leptin-dependent regulation of skeletal homeostasis. *Biochimie* **94**, 2089–2096 (2012).
34. Lecka-Czernik, B. Marrow fat metabolism is linked to the systemic energy metabolism. *Bone* **50**, 534–539 (2012).
35. Meyer, C. et al. New insights to the MLL recombinome of acute leukemias. *Leukemia* **23**, 1490–1499 (2009).
36. Du, H. Y. et al. TERC and TERT gene mutations in patients with bone marrow failure and the significance of telomere length measurements. *Blood* **113**, 309–316 (2009).
37. Townsley, D. M., Dumitriu, B. & Young, N. S. Bone marrow failure and the telomeropathies. *Blood* **124**, 2775–2783 (2014).
38. Liu, W. et al. Exosomal transfer of miR-769-5p promotes osteosarcoma proliferation and metastasis by targeting DUSP16. *Cancer Cell Int.* **21**, 541 (2021).
39. Hoffman, H., Rice, C. & Skordalakes, E. Structural analysis reveals the deleterious effects of telomerase mutations in bone marrow failure syndromes. *J. Biol. Chem.* **292**, 4593–4601 (2017).
40. Sethi, A., Ruby, J. G., Veras, M. A., Telis, N. & Melamud, E. Genetics implicates overactive osteogenesis in the development of diffuse idiopathic skeletal hyperostosis. *Nat. Commun.* **14**, 2644 (2023).
41. Nakajima, M., Koido, M., Guo, L., Terao, C. & Ikegawa, S. A novel CCDC91 isoform associated with ossification of the posterior longitudinal ligament of the spine works as a non-coding RNA to regulate osteogenic genes. *Am. J. Hum. Genet.* **110**, 638–647 (2023).
42. Chen, W. et al. New insights into the suppression of inflammation and lipid accumulation by JAZF1. *Genes Dis.* **10**, 2457–2469 (2023).
43. Li, Y. E. et al. TMEM41B and VMP1 are scramblases and regulate the distribution of cholesterol and phosphatidylserine. *J. Cell Biol.* **220**, e202103105 (2021).
44. Sekar, M. & Thirumurugan, K. Autophagy: a molecular switch to regulate adipogenesis and lipolysis. *Mol. Cell Biochem.* **477**, 727–742 (2022).
45. Uhlén, M. et al. Proteomics. Tissue-based map of the human proteome. *Science* **347**, 1260419 (2015).

46. Agrawal, S. et al. Inherited basis of visceral, abdominal subcutaneous and gluteofemoral fat depots. *Nat. Commun.* **13**, 3771 (2022).
47. Craft, C. S., Li, Z., MacDougald, O. A. & Scheller, E. L. Molecular differences between subtypes of bone marrow adipocytes. *Curr. Mol. Biol. Rep.* **4**, 16–23 (2018).
48. Labayen, I. et al. Liver fat, bone marrow adipose tissue, and bone mineral density in children with overweight. *J. Clin. Endocrinol. Metab.* **109**, e253–e258 (2023).
49. Cohen, A. et al. Increased marrow adiposity in premenopausal women with idiopathic osteoporosis. *J. Clin. Endocrinol. Metab.* **97**, 2782–2791 (2012).
50. Woods, G. N. et al. Saturated and unsaturated bone marrow lipids have distinct effects on bone density and fracture risk in older adults. *J. Bone Min. Res.* **37**, 700–710 (2022).
51. Woods, G. N. et al. Greater bone marrow adiposity predicts bone loss in older women. *J. Bone Min. Res.* **35**, 326–332 (2020).
52. Yeung, D. K. et al. Osteoporosis is associated with increased marrow fat content and decreased marrow fat unsaturation: a proton MR spectroscopy study. *J. Magn. Reson. Imaging* **22**, 279–285 (2005).
53. Justesen, J. et al. Adipocyte tissue volume in bone marrow is increased with aging and in patients with osteoporosis. *Biogerontology* **2**, 165–171 (2001).
54. Verma, S., Rajaratnam, J. H., Denton, J., Hoyland, J. A. & Byers, R. J. Adipocytic proportion of bone marrow is inversely related to bone formation in osteoporosis. *J. Clin. Pathol.* **55**, 693–698 (2002).
55. Schwartz, A. V. et al. Vertebral bone marrow fat associated with lower trabecular BMD and prevalent vertebral fracture in older adults. *J. Clin. Endocrinol. Metab.* **98**, 2294–2300 (2013).
56. Cawthorn, W. P. et al. Bone marrow adipose tissue is an endocrine organ that contributes to increased circulating adiponectin during caloric restriction. *Cell Metab.* **20**, 368–375 (2014).
57. Zhang, J. et al. Polygenic risk score added to conventional case finding to identify undiagnosed chronic obstructive pulmonary disease. *JAMA* **333**, 784–792 (2025).
58. Schunkert, H. et al. Clinical utility and implementation of polygenic risk scores for predicting cardiovascular disease. *Eur. Heart J.* **46**, 1372–1383 (2025).
59. Pachón-Peña, G. & Bredella, M. A. Bone marrow adipose tissue in metabolic health. *Trends Endocrinol. Metab.* **33**, 401–408 (2022).
60. Yu, W. et al. Bone marrow adipogenic lineage precursors promote osteoclastogenesis in bone remodeling and pathologic bone loss. *J. Clin. Invest.* **131**, e140214 (2021).
61. Kajimura, D. et al. Adiponectin regulates bone mass via opposite central and peripheral mechanisms through FoxO1. *Cell Metab.* **17**, 901–915 (2013).
62. Bydder, M. et al. Relaxation effects in the quantification of fat using gradient echo imaging. *Magn. Reson. Imaging* **26**, 347–359 (2008).
63. Salas-Ramirez, M. et al. Quantification of fat fraction in lumbar vertebrae: correlation with age and implications for bone marrow dosimetry in molecular radiotherapy. *Phys. Med. Biol.* **63**, 025029 (2018).
64. Bray, T. J., Chouhan, M. D., Punwani, S., Bainbridge, A. & Hall-Craggs, M. A. Fat fraction mapping using magnetic resonance imaging: insight into pathophysiology. *Br. J. Radiol.* **91**, 20170344 (2018).
65. Bycroft, C. et al. The UK Biobank resource with deep phenotyping and genomic data. *Nature* **562**, 203–209 (2018).
66. Littlejohns, T. J. et al. The UK Biobank imaging enhancement of 100,000 participants: rationale, data collection, management and future directions. *Nat. Commun.* **11**, 2624 (2020).
67. Liu, Y. et al. Genetic architecture of 11 organ traits derived from abdominal MRI using deep learning. *Elife* **10**, e65554 (2021).
68. Bertheau, R. C. et al. Bone marrow fat fraction assessment in regard to physical activity: KORA FF4-3-T MR imaging in a population-based cohort. *Eur. Radiol.* **30**, 3417–3428 (2020).
69. Jung, M. et al. Association of lumbar vertebral bone marrow and paraspinal muscle fat composition with intervertebral disc degeneration: 3T quantitative MRI findings from the population-based KORA study. *Eur. Radiol.* **33**, 1501–1512 (2023).
70. Loh, P. R. et al. Efficient Bayesian mixed-model analysis increases association power in large cohorts. *Nat. Genet.* **47**, 284–290 (2015).
71. Pirruccello, J. P. et al. Analysis of cardiac magnetic resonance imaging in 36,000 individuals yields genetic insights into dilated cardiomyopathy. *Nat. Commun.* **11**, 2254 (2020).
72. Wojcik, G. L. et al. Genetic analyses of diverse populations improves discovery for complex traits. *Nature* **570**, 514–518 (2019).
73. Page, G. P. et al. Multiple-ancestry genome-wide association study identifies 27 loci associated with measures of hemolysis following blood storage. *J. Clin. Invest.* **131**, e146077 (2021).
74. Winkler, T. W. et al. The influence of age and sex on genetic associations with adult body size and shape: a large-scale genome-wide interaction study. *PLoS Genet.* **11**, e1005378 (2015).
75. de Leeuw, C. A., Mooij, J. M., Heskes, T. & Posthuma, D. MAGMA: generalized gene-set analysis of GWAS data. *PLoS Comput. Biol.* **11**, e1004219 (2015).
76. Gusev, A. et al. Integrative approaches for large-scale transcriptome-wide association studies. *Nat. Genet.* **48**, 245–252 (2016).
77. Gene Ontology Consortium: going forward. *Nucleic Acids Res.* **43**, D1049–D1056 (2015).
78. Zhou, Y. et al. Metascape provides a biologist-oriented resource for the analysis of systems-level datasets. *Nat. Commun.* **10**, 1523 (2019).
79. McLaren, W. et al. The Ensembl variant effect predictor. *Genome Biol.* **17**, 122 (2016).
80. Giambartolomei, C. et al. Bayesian test for colocalisation between pairs of genetic association studies using summary statistics. *PLoS Genet.* **10**, e1004383 (2014).
81. Sebo, Z. L. et al. Bone marrow adiposity: basic and clinical implications. *Endocr. Rev.* **40**, 1187–1206 (2019).
82. Veldhuis-Vlug, A. G. & Rosen, C. J. Clinical implications of bone marrow adiposity. *J. Intern. Med.* **283**, 121–139 (2018).
83. Morris, J. A. et al. An atlas of genetic influences on osteoporosis in humans and mice. *Nat. Genet.* **51**, 258–266 (2019).
84. Karczewski, K. J. et al. Pan-UK Biobank GWAS improves discovery, analysis of genetic architecture, and resolution into ancestry-enriched effects. Preprint at *medRxiv* 2024.03.13.24303864 (2024).
85. Schoeler, T. et al. Participation bias in the UK Biobank distorts genetic associations and downstream analyses. *Nat. Hum. Behav.* **7**, 1216–1227 (2023).
86. Liu, C. G. et al. Examining the causal relationship between circulating immune cells and the susceptibility to osteomyelitis: a Mendelian randomization study. *Int. Immunopharmacol.* **131**, 111815 (2024).
87. Dönertaş, H. M., Fabian, D. K., Valenzuela, M. F., Partridge, L. & Thornton, J. M. Common genetic associations between age-related diseases. *Nat. Aging* **1**, 400–412 (2021).
88. Watson, H. J. et al. Genome-wide association study identifies eight risk loci and implicates metabo-psychiatric origins for anorexia nervosa. *Nat. Genet.* **51**, 1207–1214 (2019).
89. Ghodsian, N. et al. Electronic health record-based genome-wide meta-analysis provides insights on the genetic architecture of non-alcoholic fatty liver disease. *Cell Rep. Med.* **2**, 100437 (2021).

90. Jiang, L., Zheng, Z., Fang, H. & Yang, J. A generalized linear mixed model association tool for biobank-scale data. *Nat. Genet.* **53**, 1616–1621 (2021).
91. Suzuki, K. et al. Genetic drivers of heterogeneity in type 2 diabetes pathophysiology. *Nature* **627**, 347–357 (2024).
92. Elsworth, B. L. et al. The MRC IEU OpenGWAS data infrastructure. Preprint at *bioRxiv* <https://doi.org/10.1101/2020.08.10.244293> (2020).
93. Sakaue, S. et al. A cross-population atlas of genetic associations for 220 human phenotypes. *Nat. Genet.* **53**, 1415–1424 (2021).
94. Choi, S. W., Mak, T. S. & O'Reilly, P. F. Tutorial: a guide to performing polygenic risk score analyses. *Nat. Protoc.* **15**, 2759–2772 (2020).
95. Wang, X. & Kattan, M. W. Cohort studies: design, analysis, and reporting. *Chest* **158**, S72–s78 (2020).
96. Hemani, G. et al. The MR-Base platform supports systematic causal inference across the human phenome. *Elife* **7**, e34408 (2018).
97. Xu, W., Zhang, T., Zhu, Z. & Yang, Y. The association between immune cells and breast cancer: insights from mendelian randomization and meta-analysis. *Int. J. Surg.* **111**, 230–241 (2024).
98. Shi, Q., Wang, Q., Wang, Z., Lu, J. & Wang, R. Systemic inflammatory regulators and proliferative diabetic retinopathy: a bidirectional Mendelian randomization study. *Front. Immunol.* **14**, 1088778 (2023).
99. Verbanck, M., Chen, C. Y., Neale, B. & Do, R. Detection of widespread horizontal pleiotropy in causal relationships inferred from Mendelian randomization between complex traits and diseases. *Nat. Genet.* **50**, 693–698 (2018).
100. Zhou, W. et al. Efficiently controlling for case-control imbalance and sample relatedness in large-scale genetic association studies. *Nat. Genet.* **50**, 1335–1341 (2018).
101. Estrada, K. et al. Genome-wide meta-analysis identifies 56 bone mineral density loci and reveals 14 loci associated with risk of fracture. *Nat. Genet.* **44**, 491–501 (2012).
102. Zheng, H. F. et al. Whole-genome sequencing identifies EN1 as a determinant of bone density and fracture. *Nature* **526**, 112–117 (2015).
103. 1295433015. 1295433015/IBAS-FFCS_project: IBAS-FFCS_v1.0. Zenodo <https://doi.org/10.5281/zenodo.16519540> (2025).

Acknowledgements

This work uses data provided by patients and collected by the NHS as part of their care and support. We are grateful to all members who participated in the study, as well as all individuals who helped us complete the research. This work was supported by the Noncommunicable Chronic Diseases-National Science and Technology Major Project (2023ZD0501400), National Science Fund for Excellent Young Scholars (NSFC-82322058), the Fundamental Research Funds for the Central Universities (2042025kf0027), Program of National Natural Science Foundation of China (NSFC-82273713), National Science Fund for Distinguished Young Scholars of Hubei Province of China (2023AFA046), and Knowledge Innovation Program of Wuhan (2023020201010073) for J.T.; National Key R&D Program of China (2024YFC3405804) for X.M.; National Key R&D Program of China (2024YFC3405803) for Y.Z.; Youth

Basic Research Program of the National Natural Science Foundation of China (NSFC-824B2103) for C.N.; Key Program of National Natural Science Foundation of China (NSFC-62131009) for Q.C.; National Natural Science Foundation of China (NSFC-82202127) for J.L.

Author contributions

Z.W., J.T., Q.C., Y.Z., Z.L., and X.M. were the overall principal investigators in this study who conceived the study and obtained financial support. J.T. and Q.C. were responsible for the study design and supervised the entire study. Z.W., Y.Y., C.N., and J.L. organized the data, carried out the statistical analysis, and participated in writing the first draft of the manuscript. Z.W. designed and drew the figures. Y.C., Y.L., Z.C., S.T., J.P., Q.M., C.H., S.X., and J.C. performed the data analysis partially. All authors approved the final report for publication.

Competing interests

The authors declare no competing interests.

Additional information

Supplementary information The online version contains supplementary material available at <https://doi.org/10.1038/s41467-025-62826-3>.

Correspondence and requests for materials should be addressed to Zhen Li, Ying Zhu, Qian Chu or Jianbo Tian.

Peer review information *Nature Communications* thanks William Cawthorn, Marijana Vujković and the other, anonymous, reviewer(s) for their contribution to the peer review of this work. A peer review file is available.

Reprints and permissions information is available at <http://www.nature.com/reprints>

Publisher's note Springer Nature remains neutral with regard to jurisdictional claims in published maps and institutional affiliations.

Open Access This article is licensed under a Creative Commons Attribution-NonCommercial-NoDerivatives 4.0 International License, which permits any non-commercial use, sharing, distribution and reproduction in any medium or format, as long as you give appropriate credit to the original author(s) and the source, provide a link to the Creative Commons licence, and indicate if you modified the licensed material. You do not have permission under this licence to share adapted material derived from this article or parts of it. The images or other third party material in this article are included in the article's Creative Commons licence, unless indicated otherwise in a credit line to the material. If material is not included in the article's Creative Commons licence and your intended use is not permitted by statutory regulation or exceeds the permitted use, you will need to obtain permission directly from the copyright holder. To view a copy of this licence, visit <http://creativecommons.org/licenses/by-nc-nd/4.0/>.

© The Author(s) 2025